UNIVERSITY OF ALBERTA

Dynamic Simulation for System Response of Gearbox Including Localized Gear Faults

by

Xinhao Tian

A thesis submitted to the Faculty of Graduate Studies and Research in partial fulfillment of the requirements for the degree of Master of Science

Department of Mechanical Engineering

Edmonton, Alberta

Fall 2004

Your file Votre référence
ISBN: 0-612-95868-X
Our file Notre référence
ISBN: 0-612-95868-X

ACKNOWLEDGEMENTS

I would like to start by expressing my sincere gratitude to Dr. Ming J. Zuo and Dr. Ken R. Fyfe, excellent professors and supervisors, for giving me the opportunity to work on this interesting project, and for providing me with the guidance, support and resources necessary for accomplishing my research objectives.

My appreciation also goes to Dr. Scott D. Alexander and Dr. Don W. Raboud, who acted as my committee members, for their time of reading and examining this thesis. Their valuable suggestions helped significantly improve the quality of my work.

Special thanks are also given to the professors and office staff who have given me help and inspiration in one form or another.

My gratitude is also expressed to all group members of Reliability Research Laboratory, whose knowledge and abilities helped me a great deal.

I would like to dedicate this work to my daughter Alyshia and my wife Lifei whose love and whole-hearted support helped me to bring this work to completion. I would also like to give thanks to my father, mother and brother for encouraging me in pursuing my education.

CONTENTS

List of Tables

List of Figures

CHAPTER 1

INTRODUCTION AND BACKGROUND

1.1 Motivation

Research on dynamics of gear mechanisms has been gaining increased attention over the past several decades: from the simplest mass-spring single degree-of-freedom (SDOF) models to the complicated multiple degree-of-freedom (MDOF) dynamic models considering time-varying mesh stiffness and damping, backlash ("the lost motion between mating gear teeth" [1]), non-linearity, profile errors, friction, wear, crack and the flexibility of shafts and bearings. Models vary from considering only torsional vibration to coupling of lateral-torsional vibration, from analytical methodologies to numerical methods. However, "the ultimate goals in dynamic modeling of gears may be summarized as the study of the following: stresses; pitting and scoring; transmission efficiency; radiated noise; loads on the other machine elements of the system; stability regions; natural frequencies of the system; vibratory motion of the system; whirling of rotors; reliability and life analysis." [2]

Most of these previous studies focused on the dynamics analysis for gear design, manufacture or usage under perfect work status. Only in recent years, have the dynamic models including gear faults been developed for diagnosis

purposes. Among these studies, most of them paid more attention to the resonance response analysis or stability analysis. Few focused on the housing vibration response caused by some local gear defects.

The purpose of this work is to apply an involute gear dynamic model for fault diagnosis on the basis of the previous studies on gear dynamics. This includes two aspects:

1. The model can represent different common gear faults by pursuing the relation function between relative parameters such as stiffness, damping, contact ratio etc. and some special fault.

2. The housing vibration response due to faults should be reflected in order to further the understanding of measured vibration signals since one typically mounts accelerometers on the gearbox housing.

For the first aspect, we can consider time-varying mesh stiffness, mesh damping and/or contact ratio when some gear faults appear. The mesh stiffness is an important parameter related to the gearbox dynamics properties. Mesh stiffness variation directly affects tooth deflections and transmission error. Hence, it will cause the variation of gearbox vibration response. At the same time, gear local faults will alter the mesh stiffness during the defective tooth engagement. Therefore, gearbox vibration response may be studied by mesh stiffness variation due to tooth faults. For mesh stiffness, based on the stiffness function for perfect work condition, the mesh stiffness functions responding to chipped, cracked and broken tooth can be developed. For mesh damping, we may consider a viscous damping proportional to the mesh stiffness [4].

For the second aspect, we need to study vibration response properties of

the whole system due to fault excitation.

- Pursue analytical solutions
- Pursue numerical solutions by the use of different numerical methods.

I will apply a one-stage gear dynamic model with parameters by which different localized gear faults can be introduced. The model will consider time-varying parameters and the coupling of lateral-torsional vibration. The vibration acceleration will be the main variable of interest. I will study the accelerations on the points where the accelerometers are typically mounted (generally, they are close to the bearings.). By analytical and/or numerical methods, we can obtain vibration displacement, velocity or acceleration as a function of time/position, by which, the properties of gearbox vibration response under different tooth fault conditions can be investigated.

1.2 Literature Review

Gears are widely used in a wide variety of industries. It is one of the most common mechanisms for motion and/or power transmission from one shaft to another. The special geometrical characteristics of gear teeth will affect the dynamics and vibration of geared systems. Thus, research in the area of gear dynamics has been intensive. Many studies have focused on analyzing torsional or lateral-torsional vibration by developing involved dynamic models of geared systems, which provide us much understanding about the work status of gear systems and establish a basis for fault diagnosis of gear systems.

Dynamic modeling of gear vibration can provide us not only the vibration generation mechanisms in gear transmissions, but also the dynamic properties of various types of gear faults. With this model, we may find the vibrational

behavior of vibration sources in gear transmissions under normal or faulty conditions.

There exist three main types of mathematical models used in gear dynamics (gear dynamics is a branch of mechanics that studies how forces affect the motion of a gear system) [2].

- ***Simple Dynamic Factor Models***

Models were mainly used to determine the dynamic factors and to design gears. A dynamic factor is used in stress formulae of gear tooth root. The dynamic factor, DF, is defined as [5]

$$DF = \frac{SL}{DL} \tag{1.1}$$

where SL is the static load (a steady state load) and DL the dynamic load (the imposed in-motion force which may change in magnitude and direction). The American Gear Manufacturing Association (AGMA) [6] gave the empirical expression of DF:

$$DF = \left(\frac{78}{78 + V^{0.5}}\right)^{0.5} \tag{1.2}$$

where V is the pitch-line velocity in fpm (feet per minute) (pitch line is an ideal line in a gear, which has a common velocity with a corresponding line in the mating gear [1]). These models were built only for gear design, from which very little information about work status can be obtained.

- ***Models with Tooth Compliance***

In these models, only the gear tooth compliance is considered. The flexibility of all other elements such as shafts, bearing, etc. is neglected. The system is usually modeled as a mass-spring SDOF system.

Harris [7] considered three internal vibration sources: error in the velocity ratio due to manufacturing errors, tooth stiffness variation and tooth stiffness

nonlinearity. He seems to have been the first to observe more than one pair of mating teeth. With the aid of the photo-elastic technique, loads on all the mating teeth were measured. He pointed out that the damping would play an important role in vibration buildup. The theoretically analytical limiting value of damping ratio was 0.07 of critical. For heavy damping case, the motion is much like what one would expect from a linear system. When damping ratio is more than 0.07 of critical, nonlinearity can be neglected. The behavior of low-speed spur gears (spur gear is a gear with teeth radially arrayed on the rim parallel to its axis) could be represented in a series of static transmission error curves (the transmission error is the difference between the actual position of the mating gear and the position it would occupy if the gear drive were perfect). In experiments, however, the limiting value was about 0.1 of critical. Gregory et al. [8, 9] confirmed the theoretical results of Harris by experimental observations and computational results based on a mass-spring SDOF system. They considered sinusoidal-variation stiffness and solved the motion equations analytically for zero damping and numerically for non-zero damping. They found that the maximal dynamic load never exceeded twice the design load (the design load is the load under which a constant transmission error given) for all applied loads from no load to 1.25 times design load.

Ishida and Matsuda [10, 11] focused on the sliding friction between meshing teeth and studied the effect of friction force variation on vibration for the constant meshing stiffness. Based on a SDOF model of pitch circle (pitch circle is the centrode of the gear in meshing with the rack cutter [1]) impulse, they gave the equations of motion of system. The phase-plane method, a graphical method for solving systems of differential equations to analyze the behavior of system over time, was used for the solution. They pointed out

that the pitch circle impulse resulted from the variation of the friction force of mating teeth and was proportional to the product of angular velocity and square root of load. According to their study, the surface roughness of gear tooth has little influence on pitch circle impulse.

Lewicki [12] used a SDOF model to predict the gear life. Hertzian contact analysis was applied for the computation of mesh stiffness. For single-tooth-pair meshing, they modeled mesh stiffness of two mating teeth as two series spring stiffnesses. The corresponding equivalent stiffness was considered as a constant K during single-tooth-pair contact duration. For double-tooth-pair meshing, the total equivalent stiffness was expressed as the summation of the equivalent stiffnesses of two pairs of mating teeth, each of which was considered like that for the single-tooth-pair meshing case. The corresponding total equivalent stiffness was a constant $2K$ during double-tooth-pair contact duration.

- ***Models for gear system dynamics***

The flexibility of other elements such as the torsional flexibility of shafts and the lateral flexibility of bearings and shafts along the action line are included in such models. The vibration coupling problem between different elements has to be considered if the stiffness of these elements is relatively close to the effective mesh stiffness.

Fukuma et al. [13] studied three-directional vibrations of gears by considering the flexibility of shafts and bearings. They gave a lumped MDOF model including both lateral and torsional spring with time-varying stiffness. The Runge-Kutta-Merson process was used for numerical solution of a set of differential equations. (This method is a modification version by Merson of the Runge-Kutta method. The integration step-length h is automatically adjusted

to keep the estimated relative error per step less than a specified value ε. [14]) In their experiment, four accelerometers of piezo-electric type were applied to measure radial, axial and circumferential vibrations. They pointed out that the three-directional vibrations of spur gears were mutually coupled and the coupled coefficients were determined by the mesh stiffness of mating teeth.

In [15], Tordion and Gauvin used a 3-DOF torsional model to analyze the stability of a two-stage gear system with the same diametral pitch (the ratio of the number of gear teeth to the diameter of the gear pitch circle [1]) by assuming the rigid intermediate shaft with a gear at each end. In their study, the mesh stiffness was considered as a stepped periodic function of time. The amplitudes of the mesh stiffnesses were assumed as constants during the single- and double-tooth-pair mesh durations, respectively. The different phase variations were set by rotating one gear with respect to the other on the intermediate shaft. They showed that the frequency range of instability was greatly affected by the phase angle between the two mesh stiffnesses.

Sakai et al. [16] proposed a 5-DOF torsional model to analyze the vibration of the gear train in an automotive five-speed transmission. They considered the non-linearity of backlashes of both the gear teeth and the clutch hub splines. They found that the vibration level could be affected by the clutch modification. There existed an optimal range of clutch torsional stiffness to minimize the vibration level, which was verified by experimental studies.

Kumar et al. [17] developed a new state-space approach for solving a torsional model of a single stage spur gear system. In their study, the mesh stiffness was expressed as a five-term power series. And the damping between mating teeth was described in terms of the critical damping ratio. They pointed out that this method could greatly reduce the computation time for

obtaining a time-domain solution of the applied model by properly selecting the initial values. By this model, they investigated the variation effects of operation speed, contact position, damping and stiffness on the dynamic load. Also it was found that the damping in the system had great influence upon the stability of the system.

Lida et al. [18] used a mass-spring SDOF model to study the friction effect between gear teeth by considering the flexibility of the shaft. For simplification, only the vibration in the tooth sliding direction was considered. The vibrations in other directions were ignored. They showed that under mixed and boundary lubrication conditions, the peak amplitude of vibration response caused by the friction force between mating teeth had no relation with transmitted force and the oil viscosity. For the forced vibration, the exciting power would determine on the damping effect of the friction force.

The models coupling torsional and lateral motions are developed for various properties of gearbox vibration signals. Bartelmus [19] developed the models for one-stage gearbox system with only torsional and both torsional and lateral vibration considered. In their study, four basic factors (design, production technology, operation and condition change) in a gearing system were investigated. For one-stage system, a mass-spring-damper 8-DOF model was proposed, which included horizontal, vertical and torsional vibrations. Two constant mesh stiffnesses were used for single- and double-tooth-pair mating durations, respectively. The Runge-Kutta method was applied for obtaining the numerical solutions of the group of differential equations. It was shown that the intensity increase of tooth scuffing would result in the increase of the friction forces between mating teeth. In addition, a 6-DOF torsional model for two-stage system was also given for studying the vibration influence between

these two stages.

Howard et al. [20] studied the effects of friction and a crack using the dynamic model of a one-stage reduction gearbox. They used finite element analysis (FEA) of the whole gear body instead of the partial body model to analyze the torsional mesh stiffness (the ratio of the torque to the angular deflection) of gear teeth with and without a crack. To introduce the friction forces into the motion equations, the position, direction and value of the Coulomb friction force between mating teeth were analyzed. The position of the sliding friction force was given as a function of shaft rotation angle. The direction is always perpendicular to the action line. (Please see section 2.1 for definition of action line.) But, with the change of the contact point, the direction will be opposite with the pitch point as the change point, in which point the sliding friction force will be zero. By an FEA model, they found that the torsional mesh stiffness would be influenced by the tooth crack and the value was less than that without crack.

Yang and Lin [21] proposed a mass-spring-damper rotary model with considering tooth bending, axial compression, and Coulomb friction. A potential energy method was applied to obtain the elastic force. There existed three kinds of energies (Hertzian energy, bending energy and axial compressive energy) composing the total potential energy stored in the gear system. Among these potential energies, the bending energy is much higher than the Hertzian energy (about 4-11 times higher). The compressive energy, however, is much lower compared with other two (only about 2-3 percent of the bending energy). By this model, they investigated system responses under zero exciting torque (free vibration), constant input torque and sinusoidal input torque, respectively. Runge-Kutta method was employed to solve the dynamic equations

numerically. In addition, the calculation methods were also given for two categories of energy dissipations caused by Hertzian damping effect and friction effect of mating teeth, respectively. According to their results, the energy loss caused by the Hertzian damping effect was generally larger than that by the friction effect.

Kahraman and Singh [22] examined the frequency response characteristics of a non-linear geared rotor-bearing system with time-varying mesh stiffness by a 3-DOF model. In this model, they included a fluctuating input torque and a constant output torque. A simple sinusoidally varying mesh stiffness was used at first. They assumed the mesh damping as a sinusoidal function proportional to the mesh stiffness function. Then, it was considered as periodic function and expressed in a Fourier series form. A fifth-sixth order Runge-Kutta method was applied to pursue the numerical solutions of dynamic equations. They investigated the relation between the time-varying mesh stiffness and clearance non-linearities and found the interaction was strong between the mesh stiffness variation and gear backlash and weak between mesh stiffness and bearing non-linearities. An experimental set-up including very stiff shafts and bearings was used for testing the theoretically analytical results.

Theodossiades and Natsiavas [23] employed a 2-DOF torsional model to study dynamics of a gear system by considering backlash and time-varying mesh stiffness. A Fourier series form was used for describing the gear mesh stiffness. For a specific small frequency range of interest, say the gear mesh frequency or its harmonics, and small mesh stiffness variation, approximate periodic solutions were obtained by using approximate analytical methodologies. Numerical methods were employed to verify the analytical results. In addition, the effect of the mesh stiffness variation on the gear-pair periodic

response was also investigated. Relatively large mesh stiffness variation will strengthen the influence on the response. For the damping parameter, they found that the larger the damping, the smaller the response amplitude.

Amabili and Rivola [4] used an SDOF torsional model to investigate the steady-state response of a pair of spur gears with low contact ratio (between 1 and 2) by considering a time-varying mesh stiffness and a viscous damping proportional to the mesh stiffness. In theoretical analysis, the mesh stiffness was expressed as a complex Fourier series. For simplicity, they considered only the first two terms of the Fourier expansion. A closed-form solution was obtained at any rotation speed without tooth separation. In the numerical simulation, they used the mesh stiffness function proposed by Cai and Hayashi [24], which could be calculated by:

$$k(t) = \frac{\left[\frac{-1.8}{(\epsilon T)^2}t^2 + \frac{1.8}{\epsilon T}t + 0.55\right]}{0.85\epsilon}k_m \tag{1.3}$$

where k_m is the integral average stiffness of gear pair, T the gear meshing period, and ϵ contact ratio. In their experimental study, a pair of involute spur gears with same tooth number 48, module $4mm$ and pressure angle 14.5° were employed. The contact ratio ϵ was 1.8. The corresponding vibration acceleration response of the driven gear was obtained under different rotation speeds of the driving gear. They pointed out that in order to accurately describe the vibration acceleration response at relatively low speed, more harmonics had to be considered in the expansion of the Fourier series used for the mesh stiffness expression.

Parker et al. [25, 26] investigated the dynamic response of a spur and a planetary gear pair using a unique finite element/contact mechanics model.

This method overcame the limitation of traditional FEA in gear dynamic analysis for components away from the tooth mesh part. For the area near the tooth contact surface, the analytical solution was obtained. For the area slightly away from the contact surface, however, they pursued the finite element solution. The mesh stiffness was approximated as a rectangular wave where the sudden change points corresponded to the alternations of the number of mating tooth pairs. The mesh damping ratio was selected as 0.08. In the experimental studies, a pair of identical spur gears with 50 teeth, module $3mm$ and pressure angle 20° were used. The contact ratio was 1.75. The natural frequency was investigated. It was found that there existed a weak relation between the natural frequency and load.

Kuang and Lin [27] studied the effect of tooth wear on the vibration response of a pair of spur gears by considering the load sharing alternation, position dependent mesh stiffness, damping factor and friction coefficient. The mesh stiffness was approximately expressed as a function of the gear tooth numbers, the loading position, the pitch circle radius, the gear modification coefficient and the module of gears. A constant damping ratio 0.17 was used in their analysis. An approximate formula was employed to calculate the accumulative wear depth at some point after n mesh cycles. In their study, a pair of steel spur gears with tooth numbers 29 and 57, pressure angle 20°, and the module $4mm$ were investigated. Results showed that the dynamic load and the velocity at the tooth mating point had important influence on the sliding wear, which changed the profiles of mating teeth and load distribution. The dynamic load magnitude had only a weak relationship with the sliding wear within the first 10^5 running cycles. The transmitted torque spectra illustrated that the peak amplitude was located at the fifth harmonic of the mesh fre-

quency. As the sliding wear progressed, the amplitudes of the lower harmonics of the mesh frequency increased drastically, but the peak amplitude had a very slight increase.

In [28], Kuang and Lin theoretically analyzed the dynamic behavior of a pair of spur gears and indicated the effect of the time-varying mesh stiffness on the vibration spectrum of a transmitted torque. In the proposed model, they included the amplitude modulation excited by the tooth error and the driving torque fluctuation. Two constant values, k_d and k_s corresponding to double- and single-tooth-pair mesh durations, respectively, were used to approximate the mesh stiffness k_m in a mesh period. In their numerical study, they focused on the influence of the input torque fluctuation by employing the same pair of steel gears as those used in [27]. The results were obtained by the comparison of the corresponding amplitude spectra of the transmitted torques under constant and harmonically fluctuated input torques. For the constant input torque, the spectra consisted of the harmonics of the mesh frequency and dominated by fifth and sixth harmonics, which coincided with the first resonance frequency of the gear set used. Comparatively, for a sinusoidally fluctuated torque with the shaft rotational frequency, the amplitude of the transmitted torque was enhanced and sideband frequency components appeared at both sides of the harmonics of the mesh frequency. The difference between the main spectral line and the corresponding sideband was the shaft rotating frequency, which was also displayed in the frequency spectrum. In addition, when the effect of tooth profile error was considered at the same time, the fluctuation amplitude increased again. Also, a peak line at the second harmonic of the mesh frequency was observed.

Badaoui et al. [29] presented a 6-DOF model for the dynamic response sim-

ulation of the spur and helical gear systems with the effect of tooth spalling defect. In their model, the gears were simulated as two rigid cylinders. For simplification, the variations of the gear mesh stiffness along defect widths were not considered. They pointed out that small-depth tooth defects caused the external exciting forces, which were roughly proportional to the volume of spalling part, i.e. the product of the average of depth and width of defect. Deeper defects, however, would have an influence on the mesh stiffness. From the investigation on the positions of defects, it was found that the detectability of small defects was independent of their positions on the tooth profiles, whereas it was easier to detect larger defects in the central part of tooth profile.

Lin and Parker [30] used a mass-spring 3-DOF torsional model of a two-stage gear train to investigate the effect of mesh stiffness variation with rectangular waveforms on the vibration response under different mesh frequencies, amplitudes of mesh stiffness variation, contact ratios, and mesh phasing between two stages. In their study, the mesh stiffness was approximately expressed as a Fourier series with the first three terms. Results showed that mesh phasing and contact ratio have a great influence on the system instability (corresponding to the system resonance). If damping was taken into consideration, the system stability would improve. According to their study, when the contact ratio was between 1.4 and 1.6, it was found that the dynamic stability of one-stage gears at high speeds was compromised. Therefore, the reduction of dynamic instability could be fulfilled by properly selecting contact ratio and mesh phasing. In addition, for the two-stage case, when one mesh frequency was an integer multiple of the other, there existed interaction between the vibration responses from the two meshes. The instability would significantly change in comparison with no interaction case corresponding to

no integer multiple relation between two mesh frequencies.

Lee et al. [31] applied a finite element model of a gear pair considering both lateral and torsional vibration to investigate the vibration characteristics of a speed-increasing gear system. They investigated the mode shapes with varying gear mesh stiffness. The gear mesh damping was neglected in their study. The relationship between natural frequencies of system and the gear mesh stiffness was carried out. For the uncoupled case, the first three torsional natural frequencies increased as the gear mesh stiffness increased over a certain value while the lateral natural frequencies remained unchanged. Among these three natural frequencies, the first two increased sharply with certain ranges of the mesh stiffness and thereafter nearly constants. The third, however, increased slowly. In comparison with the uncoupled results, for the coupled case, the second torsional natural frequency reduced greatly. the lateral high order natural frequencies slightly increased with the mesh stiffnesses over some values. By mode analysis, it was found that as the gear mesh stiffness increased over a certain value, the dominant mode might exchange between the torsional one and the lateral one.

Wojnarowski and Onishcheko [32] investigated the effect of the tooth deformation and wear on gear dynamics analytically and experimentally by employing a 2-DOF involute tooth model. The mathematical expressions of the curves of the unworn and worn tooth outlines were given. They considered the tooth outline changes (which cause the instantaneous gear ratio changes) due to the wear of tooth. (The gear ratio is the ratio of instantaneous angular velocities of two mating gears [1].) The outline of the worn tooth was approximated by a continuous polynomial function. It was found that the wear was not the same along the profile curve of the tooth. The profile of the tooth

would not remain involute at a serious wear. At the same time, the shape of the action line would not be a straight line corresponding to a pair of perfect gears.

1.3 Summary

The previously-mentioned literature on modeling of gear systems contains three main groups of the mathematical models developed and applied in gear dynamics. In general, the purposes of modeling are to study the gear tooth stresses, natural frequencies of the system, vibration characteristics of the gear system such as amplitudes and spectral components, noise radiation, transmission efficiency of the system, stability of the system and life cycles. According to the different objectives, mass-spring or mass-spring-damper SDOF/MDOF models of one/two-stage gear trains are used. Only the torsional vibrations of systems are usually considered in relatively earlier studies. Thereafter, models considering lateral vibrations or both torsional and lateral vibrations are developed. In these models, the gear mesh stiffness is considered as a constant, a simple sinusoidal function, a Fourier series, a rectangular waveform corresponding to the single- and double-tooth-pair meshes, an approximation function or a derivative expression. In the solution of dynamic equations, analytical, approximately analytical or numerical methods are employed. For some very simple SDOF mathematical models, closed form solutions are obtained. For more complicated models, approximate analytical solutions are given. For complicated MDOF system models, especially when both torsional and lateral vibrations considered, numerical techniques have to be employed usually. Among these numerical methods, Runge-Kutta integration techniques are more popular due to the accuracy and calculation time required.

1.4 Goal of Research

Among the past studies, most of them focused on the stability analysis of the gear system. Few concentrated more attention on the mechanism and characteristics of the housing vibration response with some local tooth defects, which are helpful to the fault analysis of the practically applied gearbox since most observed vibration signals are typically collected from the gearbox housing. The gear mesh stiffness analysis, by which local tooth defects can be introduced analytically, will contribute to the understanding of the vibration response mechanism and characteristics of gearbox.

1.5 Organization of Thesis

The thesis is organized as follows. Relevant literature is surveyed in Chapter 1, and the calculation method of the effective mesh stiffness is given in Chapter 2. Chapter 3 is devoted to the introduction of gear local faults by considering stiffness changes. The results of the dynamics simulation of gear local faults are presented in Chapter 4. Finally, there are summaries and future recommendations in Chapter 5.

Chapter 2

Mesh Stiffness of Sound Gears

2.1 Introduction

In this thesis, involute spur gears will be investigated as the involute spur tooth profile is the most commonly used type for gearing today. An involute is a curve traced by a point on a taut cord unwinding from a circle, called a Base Circle.

Figure 2.1 shows the technical nomenclature of involute spur gears. Between a pair of meshing gears, the smaller gear is called the pinion while the larger engaged by the pinion is called the gear. The outside circle is a circle formed by tooth tips. The radial distance between the outside circle and the pitch circle is the addendum. For standard involute gears, the addendum is equal to the reciprocal of the diametral pitch (symbolized as P), which is the number of teeth of a gear per inch of the diameter of the pitch circle. For a pair of mating gears, their diametral pitches are the same.

In Figure 2.1, point P is the tangency point of pitch circles, also called the pitch point. Line $t-t$ is the common tangent to pitch circles. Line B_1B_2 is the action line, the common tangent to the base circles and the common normal to the tooth profiles. The angle α_0 between lines $t-t$ and B_1B_2 is called the

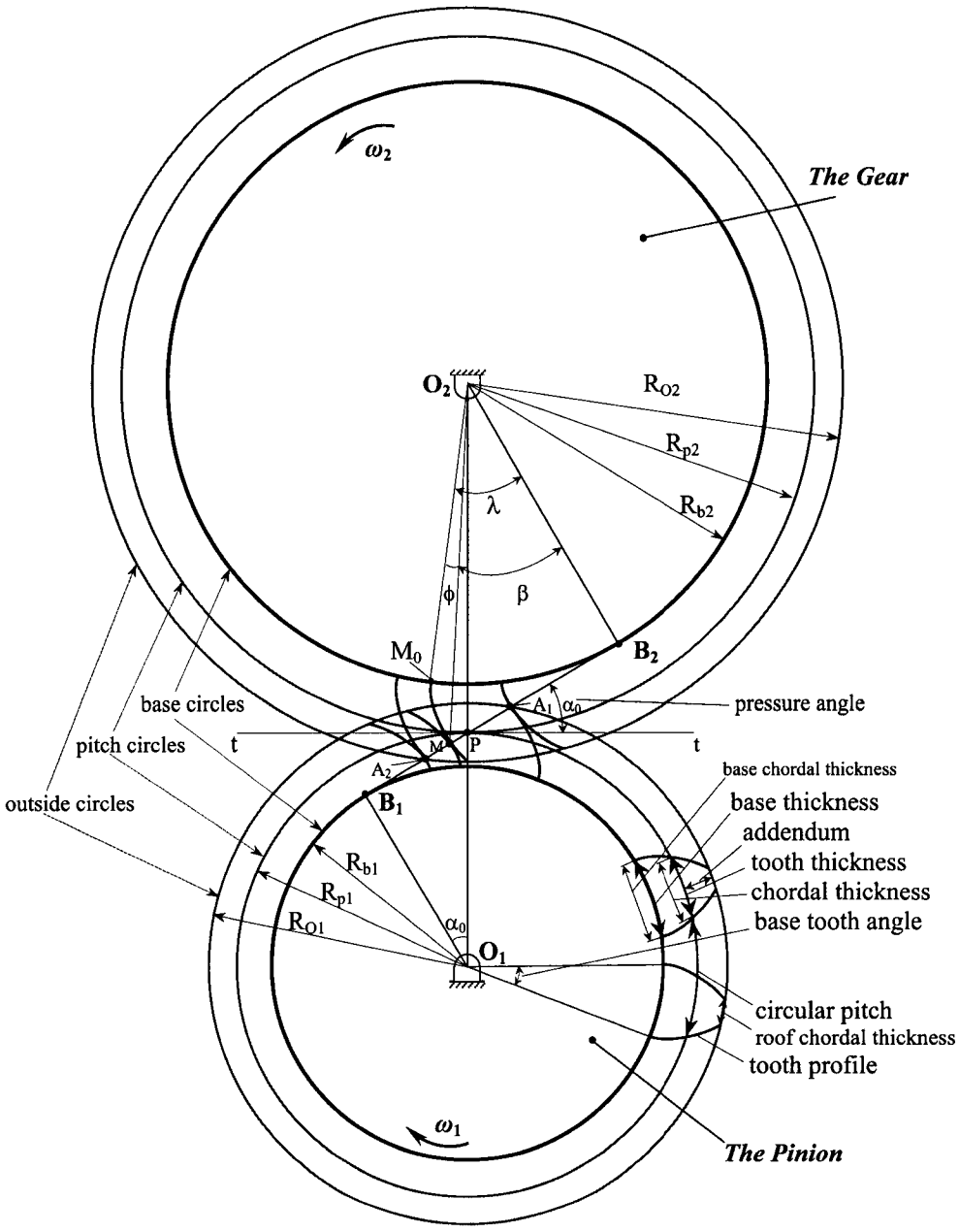

Figure 2.1: Involute-gear nomenclature

standard pressure angle. The most commonly used pressure angles for spur gears are 14.5°, 20° and 25° [1, 3].

Points A_2, M and A_1, corresponding to three meshing positions of a pair of tooth profiles, are three contact points on the action line. For involute gears, contact points of a pair of mating teeth are always along the action line. Point A_2 represents the contact point in the beginning of meshing. Point M is the current position of the contact point. Point A_1 represents the contact position in the end of meshing for the same pair of tooth profiles. Line segment $\overline{A_2A_1}$, which is called the working part of the action line, indicates the locus of contact points of a pair of mating teeth. It can be calculated as:

$$\overline{A_2A_1} = \sqrt{R_{O1}^2 - R_{b1}^2} + \sqrt{R_{O2}^2 - R_{b2}^2} - \overline{O_1O_2}\sin\alpha_0 \tag{2.1}$$

where R_{O1}, R_{O2}, R_{b1} and R_{b2} are the radii of outside and base circles of the pinion and the gear, respectively. $\overline{O_1O_2}$ is the center distance, which is the distance between the rotation centers O_1 and O_2 of the pinion and the gear.

R_{b1}, R_{b2}, R_{O1}, R_{O2} and $\overline{O_1O_2}$ can be expressed as follows, [1, 3]

$$R_{b1} = \frac{N_1}{2P}\cos\alpha_0 \tag{2.2}$$

$$R_{b2} = \frac{N_2}{2P}\cos\alpha_0 \tag{2.3}$$

$$R_{O1} = \frac{N_1 + 2}{2P} \tag{2.4}$$

$$R_{O2} = \frac{N_2 + 2}{2P} \tag{2.5}$$

$$\overline{O_1O_2} = \frac{N_1 + N_2}{2P} \tag{2.6}$$

where N_1 and N_2 are the tooth numbers of the pinion and the gear, respectively,

and P the diametral pitch.

For an involute tooth profile $\widehat{M_0M}$ shown in Figure 2.1, the relations of the related angles ϕ, β and λ, arc $\widehat{M_0B_2}$, line segment $\overline{B_2M}$, and the base radius R_{b2} of the gear are as follows.

$$\overline{B_2M} = \lambda R_{b2} = R_{b2} \tan\beta \tag{2.7}$$

Equation (2.7) can be simplified as:

$$\lambda = \tan\beta \tag{2.8}$$

From Equation (2.8), the angle ϕ can be expressed as:

$$\phi = \lambda - \beta = \tan\beta - \beta \tag{2.9}$$

Function $\phi(\beta)$ is designated as $\boldsymbol{inv}\beta$ (called the involute function), i.e.

$$\boldsymbol{inv}\beta = \tan\beta - \beta \tag{2.10}$$

The purpose of this work is to simulate the system response of gearbox including different common gear faults by pursuing the relation function between relative parameters and some special fault. The system vibration response is caused by the contact load of meshing gear teeth, which varies as the contact point moves along the action line, while the contact load is mainly caused by single/double-tooth-pair contact transitions and mesh stiffness variation along the contact. Therefore, it is necessary to study the mesh stiffness variation along the contact. In this chapter, we will provide the calculation method

based on the energy method.

2.2 Calculation Method of Mesh Stiffness

We will consider the mesh stiffness of a pair of involute spur gears (meshing as shown in Figure 2.2) without manufacturing error. The stiffnesses of all other gearbox components will be considered in Chapter 4. It is assumed that the lubrication condition is perfect such that the friction is ignored in this study. For the purpose of simplification in calculating the mesh stiffness, only the stiffness of the meshing gears are considered. All other system components are considered rigid. The error in the mesh stiffness due to this simplification can be ignored since what we are concerned about is the difference between the faulty case and the perfect case.

Yang and Lin [21] proposed the potential energy method, which can be used for the calculation of the effective stiffness. They pointed out that the total potential energy stored in the meshing gear system included three parts: the Hertzian energy, the bending energy and the axial compressive energy, which can be used for the calculations of the Hertzian contact stiffness, the bending stiffness and the axial compressive stiffness, respectively. However, they did not consider the shear energy, which will be included in this study. The details will be given in Sections 2.2.1 and 2.2.2.

2.2.1 Calculation of Hertzian Contact Stiffness

In this study, it is assumed that the mating teeth are two isotropic elastic bodies. Yang and Sun [33] stated that "According to Hertzian law, the elastic compression of two isotopic elastic bodies can be approximated by two paraboloids in the vicinity of the contact. The error of this approximation will

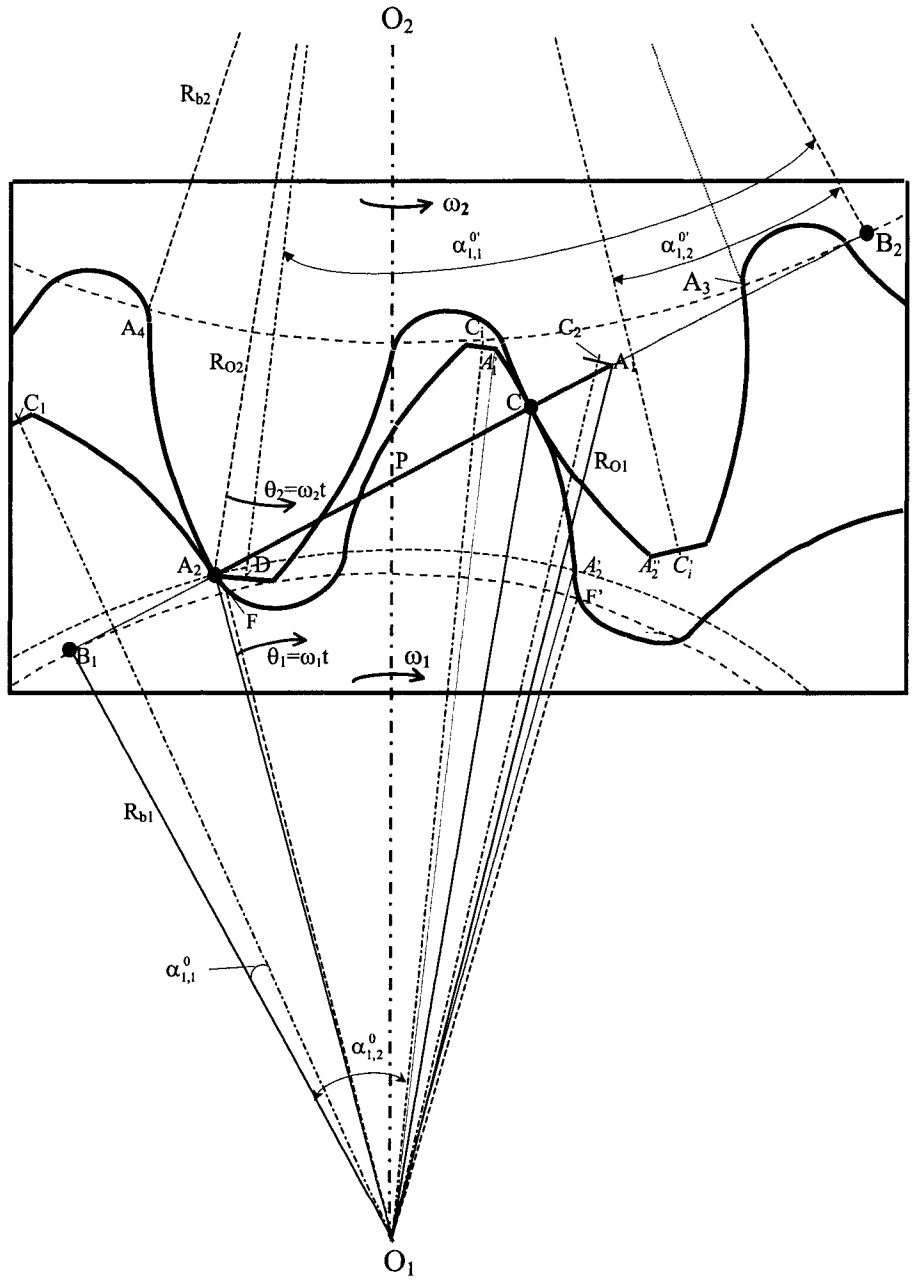

Figure 2.2: A gear-meshing sketch of a pair of gears

be less than 0.5 percent." According to their analysis, the Hertzian-contact stiffness of a pair of meshing teeth made of the same material is a constant along the entire action line. It is independent of the contact position. This constant can be expressed as [33]:

$$k_h = \frac{\pi EL}{4(1-\nu^2)} \tag{2.11}$$

where E, L, ν represent Young's modulus (a constant describing the stiffness property of material), the width of tooth, and Poisson's ratio (an elastic constant describing the compressibility of material), respectively. From this expression, it is observed that when the tooth width changes, k_h will change correspondingly. For a perfect gear, the width of the effective work surface will remain unchanged.

The Hertzian energy is the potential energy stored in the vicinity of contact point because of the elastic deformation of the teeth and can be calculated from:

$$U_h = \frac{F^2}{2k_h} \tag{2.12}$$

where F represents the acting force by the mating tooth in the contact point and k_h the effective Hertzian stiffness in the same direction with the force F.

2.2.2 Calculation of Bending, Shear and Axial Compressive Stiffnesses

The bending, shear and axial compressive energies stored in a tooth can be expressed as [21]:

$$U_b = \frac{F^2}{2k_b} \tag{2.13}$$

$$U_s = \frac{F^2}{2k_s} \tag{2.14}$$

$$U_a = \frac{F^2}{2k_a} \tag{2.15}$$

where k_b, k_s and k_a represent the effective bending, shear and axial compressive stiffnesses in the same direction with the force F, respectively.

According to the properties of involute profile, the action line is the common normal to the tooth profiles. Correspondingly, the acting force F of the contact teeth should be always along the action line. Thus, F can be resolved into two perpendicular component forces, F_b and F_a (refer to Figure 2.3), which can be calculated as:

$$F_b = F\cos\alpha_1 \tag{2.16}$$

$$F_a = F\sin\alpha_1 \tag{2.17}$$

As shown in Figure 2.3, F_b provides bending and shear effects, while F_a causes both axial compressive and bending effect. The torque M represents the bending effect of F_a. It can be expressed as:

$$M = F_a h \tag{2.18}$$

where h is the distance between the contact point and the central line of the tooth, which can be obtained as follows (refer to Equation (10) in [21]):

$$h = R_b[(\alpha_1 + \alpha_2)\cos\alpha_1 - \sin\alpha_1] \tag{2.19}$$

where α_2 represents the half of the base tooth angle (please see Figure 2.1 on page 19 for the base tooth angle).

According to the geometry of the involute tooth, in Figure 2.3, the distance

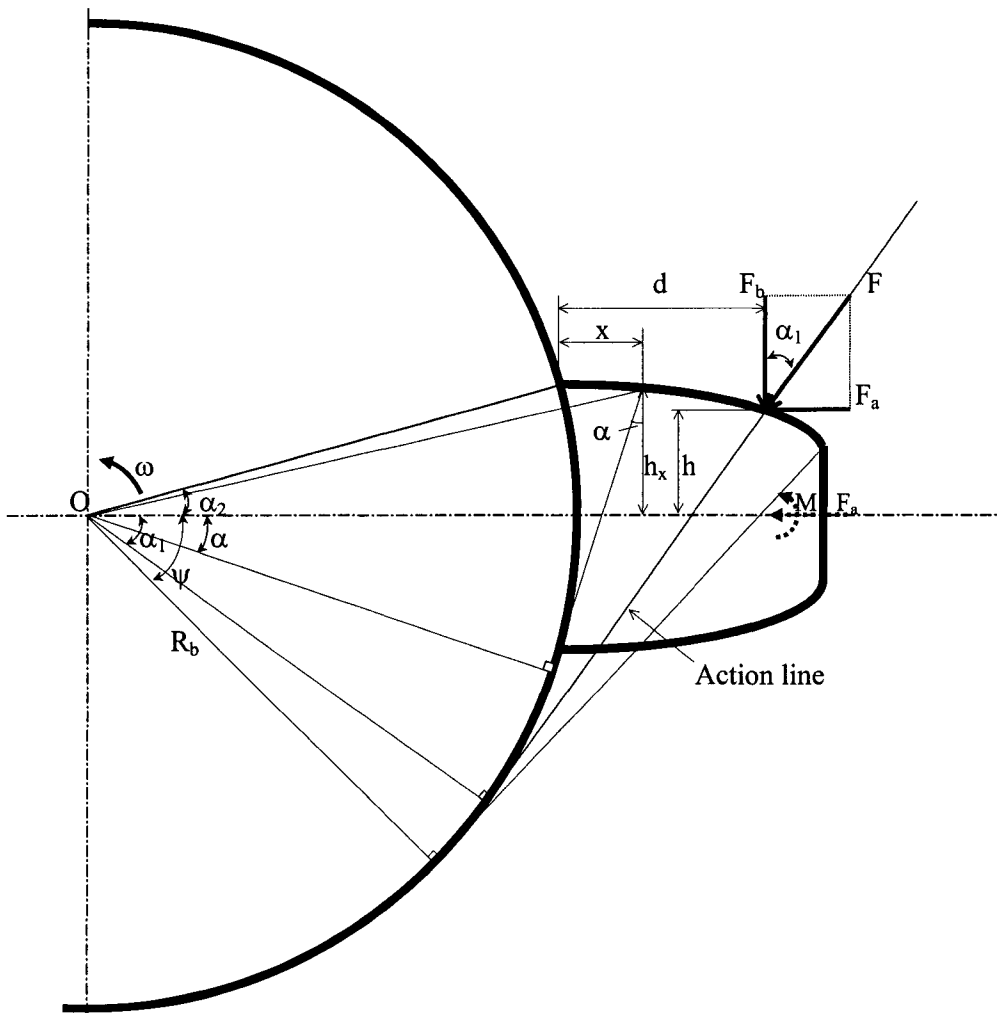

Figure 2.3: Elastic force on a tooth

d between the contact point and the tooth root can be expressed as (refer to Equation (11) in [21]):

$$d = R_b[(\alpha_1 + \alpha_2)\sin\alpha_1 + \cos\alpha_1 - \cos\alpha_2] \tag{2.20}$$

In this study, the tooth on the gear is modeled as a cantilevered beam. It is assumed that the base of the beam (at the root of the tooth) does not experience any deflection. [21]

The bending potential energy, based on beam theory, can be obtained by (refer to Equation (14) in [21]):

$$U_b = \int_0^d \frac{[F_b(d-x) - M]^2}{2EI_x} dx \tag{2.21}$$

where I_x represents the area moment of inertia of the section where the distance from the tooth root is x. It can be calculated as:

$$I_x = \frac{1}{12}(2h_x)^3 L = \frac{2}{3}h_x^3 L \tag{2.22}$$

where h_x is the distance between the point on the tooth curve corresponding to the section where the distance from the tooth root is x and the central line of the tooth, which can be obtained as follows (refer to Equation (2.19) on page 25):

$$h_x = R_b[(\alpha + \alpha_2)\cos\alpha - \sin\alpha] \tag{2.23}$$

To investigate the parameter properties at some angular displacement of the pinion/gear (angular displacement is the angle that the pinion/gear goes through from the initial reference point), it will be more convenient to express the relationship as angular variables (reflecting the angle) instead of linear

ones (reflecting the length). From the geometry of involute profile, x can be expressed as:

$$x = R_b[\cos\alpha - (\alpha_2 - \alpha)\sin\alpha - \cos\alpha_2] \tag{2.24}$$

Differentiate Equation 2.24, dx can be calculated as:

$$dx = R_b(\alpha - \alpha_2)\cos\alpha d\alpha \tag{2.25}$$

Now, instead of x, α becomes the integration variable. Substitute U_b in Equation (2.13) into the left side of Equation (2.21), and substitute F_b, M, d, I_x, x, and dx in Equations (2.16), (2.18), (2.20), (2.22), (2.24) and (2.25) into the right side of Equation (2.21). After simplification, the result will be:

$$\frac{1}{k_b} = \int_{-\alpha_1}^{\alpha_2} \frac{3\{1 + \cos\alpha_1[(\alpha_2 - \alpha)\sin\alpha - \cos\alpha]\}^2(\alpha_2 - \alpha)\cos\alpha}{2EL[\sin\alpha + (\alpha_2 - \alpha)\cos\alpha]^3} d\alpha \tag{2.26}$$

Correspondingly, the shear energy can be expressed as (refer to Equation (4-3.11) in [39]):

$$U_s = \int_0^d \frac{1.2{F_b}^2}{2GA_x} dx \tag{2.27}$$

where G is the shear modulus, which can be expressed as (refer to Equation (2-10) in [40]):

$$G = \frac{E}{2(1+\nu)} \tag{2.28}$$

In Equation (2.27), A_x is the area of the section, which can be calculated as:

$$A_x = 2h_x L \tag{2.29}$$

Substitute U_s in Equation (2.14) into the left side of Equation (2.27), and substitute F_b, dx, G and A_x in Equations (2.16), (2.25), (2.28) and (2.29) into

the right side of Equation (2.27). The result is as follows:

$$\frac{1}{k_s} = \int_{-\alpha_1}^{\alpha_2} \frac{1.2(1+\nu)(\alpha_2-\alpha)\cos\alpha\cos^2\alpha_1}{EL[\sin\alpha+(\alpha_2-\alpha)\cos\alpha]}d\alpha \tag{2.30}$$

In a similar way, the axial compressive energy can be expressed as (refer to Equation (15) in [21]):

$$U_a = \int_0^d \frac{{F_a}^2}{2EA_x}dx \tag{2.31}$$

Substitute U_a in Equation (2.15) into the left side of Equation (2.31), and substitute F_a, dx, and A_x in Equations (2.17), (2.25) and (2.29) into the right side of Equation (2.31). The result is as follows:

$$\frac{1}{k_a} = \int_{-\alpha_1}^{\alpha_2} \frac{(\alpha_2-\alpha)\cos\alpha\sin^2\alpha_1}{2EL[\sin\alpha+(\alpha_2-\alpha)\cos\alpha]}d\alpha \tag{2.32}$$

Equations (2.26), (2.30) and (2.32) show that given a pair of meshing teeth with involute profile, the bending, shear and compressive stiffnesses will only be functions of α_1, which determines the position of contact point along the tooth surfaces.

The summation of Hertzian, bending, shear and axial compressive energies will constitute the total potential energy stored in a single pair of meshing teeth, which can be expressed as (refer to Equation (28) in [21]):

$$\begin{aligned} U_t = \frac{F^2}{2k_t} &= U_h + U_{b1} + U_{s1} + U_{a1} + U_{b2} + U_{s2} + U_{a2} \\ &= \frac{F^2}{2}\left(\frac{1}{k_h} + \frac{1}{k_{b1}} + \frac{1}{k_{s1}} + \frac{1}{k_{a1}} + \frac{1}{k_{b2}} + \frac{1}{k_{s2}} + \frac{1}{k_{a2}}\right) \end{aligned} \tag{2.33}$$

where k_t represents the total effective mesh stiffness of a pair of meshing teeth

in the same direction with the force F, which can be calculated as:

$$k_t = \frac{1}{\frac{1}{k_h} + \frac{1}{k_{b1}} + \frac{1}{k_{s1}} + \frac{1}{k_{a1}} + \frac{1}{k_{b2}} + \frac{1}{k_{s2}} + \frac{1}{k_{a2}}} \tag{2.34}$$

In Equations (2.33) and (2.34), subscripts 1 and 2 represent the pinion and the gear, respectively.

So far, the calculation formulas (Equations (2.11), (2.26), (2.30), (2.32) and (2.34)) of mesh stiffnesses as the functions of angular variable α_1 have been obtained based on the potential energy method [21].

2.3 Mesh Stiffness of Double/Single-tooth-pair Meshing Duration

In this section, we will derive the calculation expressions of mesh stiffness for the double/single-tooth-pair meshing duration.

For a pair of meshing gears whose contact ratio varies between 1 and 2, the mesh stiffness variation during the tooth engagement mainly includes two aspects: the stiffness variation during single-tooth-pair mesh and that during double-tooth-pair mesh. For this purpose, the mesh period has to be investigated in detail as the number of mating tooth pairs is not a constant during the entire meshing period. It is necessary to know the relationship of the number of meshing tooth pair and the angle displacement of the pinion/gear. Further, the corresponding stiffness under any angular displacement of the shaft can be calculated.

Refer to Figure 2.2. In this study, we define the mating tooth pair on the left side as "the first pair" and that on the right side as "the second pair" when there are two pairs of teeth meshing simultaneously.

2.3.1 Mesh Stiffness Calculation

Given k_h, k_b, k_s and k_a, based on Equation (2.34), the total effective stiffness can be calculated according to Equation (2.35) for each pair of meshing teeth.

$$k_{t,i} = \frac{1}{\frac{1}{k_h} + \frac{1}{k_{b1,i}} + \frac{1}{k_{s1,i}} + \frac{1}{k_{a1,i}} + \frac{1}{k_{b2,i}} + \frac{1}{k_{s2,i}} + \frac{1}{k_{a2,i}}}, \qquad i = 1, 2 \tag{2.35}$$

The stiffnesses $k_{b1,i}$, $k_{s1,i}$, $k_{a1,i}$, $k_{b2,i}$, $k_{s2,i}$ and $k_{a2,i}$ can be expressed as follows (refer to Equations (2.26), (2.30) and (2.32)):

$$\frac{1}{k_{b1,i}} = \int_{-\alpha_{1,i}}^{\alpha_2} \frac{3\{1 + \cos\alpha_{1,i}[(\alpha_2 - \alpha)\sin\alpha - \cos\alpha]\}^2(\alpha_2 - \alpha)\cos\alpha}{2EL[\sin\alpha + (\alpha_2 - \alpha)\cos\alpha]^3} d\alpha \tag{2.36}$$

$$\frac{1}{k_{s1,i}} = \int_{-\alpha_{1,i}}^{\alpha_2} \frac{1.2(1+\nu)(\alpha_2 - \alpha)\cos\alpha\cos^2\alpha_{1,i}}{EL[\sin\alpha + (\alpha_2 - \alpha)\cos\alpha]} d\alpha \tag{2.37}$$

$$\frac{1}{k_{a1,i}} = \int_{-\alpha_{1,i}}^{\alpha_2} \frac{(\alpha_2 - \alpha)\cos\alpha\sin^2\alpha_{1,i}}{2EL[\sin\alpha + (\alpha_2 - \alpha)\cos\alpha]} d\alpha \tag{2.38}$$

$$\frac{1}{k_{b2,i}} = \int_{-\alpha'_{1,i}}^{\alpha'_2} \frac{3\{1 + \cos\alpha'_{1,i}[(\alpha'_2 - \alpha)\sin\alpha - \cos\alpha]\}^2(\alpha'_2 - \alpha)\cos\alpha}{2EL[\sin\alpha + (\alpha'_2 - \alpha)\cos\alpha]^3} d\alpha \tag{2.39}$$

$$\frac{1}{k_{s2,i}} = \int_{-\alpha'_{1,i}}^{\alpha'_2} \frac{1.2(1+\nu)(\alpha'_2 - \alpha)\cos\alpha\cos^2\alpha'_{1,i}}{EL[\sin\alpha + (\alpha'_2 - \alpha)\cos\alpha]} d\alpha \tag{2.40}$$

$$\frac{1}{k_{a2,i}} = \int_{-\alpha'_{1,i}}^{\alpha'_2} \frac{(\alpha'_2 - \alpha)\cos\alpha\sin^2\alpha'_{1,i}}{2EL[\sin\alpha + (\alpha'_2 - \alpha)\cos\alpha]} d\alpha \tag{2.41}$$

where i=1 for the first pair of meshing teeth when there are two pairs of teeth meshing, i=2 for the second pair. α_2 and α'_2 are the half tooth angles on

the base circles of the pinion and the gear, respectively, which are constants for a given gear pair and can be calculated as Equations (2.42) and (2.43), respectively [3] (refer to Figures 2.2 and 2.3).

$$\alpha_2 = \angle C_i O_1 F = \frac{\pi}{2N_1} + \boldsymbol{inv}\alpha_0 \tag{2.42}$$

$$\alpha_2' = \angle C_i' O_2 A_3 = \frac{\pi}{2N_2} + \boldsymbol{inv}\alpha_0 \tag{2.43}$$

where N_1 and N_2 are the numbers of teeth of the pinion and the gear, respectively.

For the first pair of meshing teeth, given a contact point M (as shown in Figure 2.1 on page 19), we can derive the equations of the angles $\alpha_{1,1}$ (corresponding to the angle α_1 of the pinion) and $\alpha_{1,1}'$ (corresponding to the angle α_1 of the gear) (refer to Figure 2.3).

Consider point A_2 shown in Figure 2.2 as the reference point, which corresponds to the initial meshing point of the first pair of meshing teeth. At this point, the angular displacements of the meshing gears, θ_1 and θ_2, are both zero. The corresponding angle $\alpha_{1,1}^0$ can be expressed as (refer to Figure 2.2):

$$\alpha_{1,1}^0 = \angle B_1 O_1 C_1 = \angle B_1 O_1 A_2 - \angle C_1 O_1 A_2 \tag{2.44}$$

where $\angle B_1 O_1 A_2$ can be calculated as:

$$\angle B_1 O_1 A_2 = \arccos \frac{R_{b1}}{\overline{O_1 A_2}} \tag{2.45}$$

In Equation (2.45), $\overline{O_1 A_2}$ can be obtained by:

$$\overline{O_1 A_2} = \sqrt{R_{O2}^2 + \overline{O_1 O_2}^2 - 2R_{O2}\overline{O_1 O_2}\cos\angle O_1 O_2 A_2} \tag{2.46}$$

where $\angle O_1O_2A_2$ can be calculated as:

$$\angle O_1O_2A_2 = \arccos\frac{R_{b2}}{R_{O2}} - \alpha_0 \tag{2.47}$$

In Equation (2.44), $\angle C_1O_1A_2$ can be expressed as:

$$\begin{aligned}\angle C_1O_1A_2 &= \angle C_1O_1F - \angle A_2O_1F \\ &= \alpha_2 - \boldsymbol{inv}\angle B_1O_1A_2\end{aligned} \tag{2.48}$$

Now substitute $\angle C_1O_1A_2$ in Equation (2.48) into Equation (2.44) to obtain (recall Equation (2.10) on page 21):

$$\alpha^0_{1,1} = \angle B_1O_1A_2 - \alpha_2 + \boldsymbol{inv}\angle B_1O_1A_2 = \tan\angle B_1O_1A_2 - \alpha_2 \tag{2.49}$$

Combine Equations (2.42), (2.45)-(2.47) and (2.2)-(2.6) with Equation (2.49). After simplification, the angle $\alpha^0_{1,1}$ is found from,

$$\alpha^0_{1,1} = -\frac{\pi}{2N_1} - \boldsymbol{inv}\alpha_0 + \tan\left[\arccos\frac{N_1\cos\alpha_0}{\sqrt{(N_2+2)^2+(N_1+N_2)^2-2(N_2+2)(N_1+N_2)\cos(\arccos\frac{N_2\cos\alpha_0}{N_2+2}-\alpha_0)}}\right] \tag{2.50}$$

Equation (2.50) gives the calculation formula of the angle $\alpha_{1,1}$ when the angular displacement of the pinion is zero. When the angular displacement of the pinion is θ_1 (as shown in Figure 2.2), the angle $\alpha_{1,1}$ will be:

$$\alpha_{1,1} = \theta_1 + \alpha^0_{1,1} = \theta_1 - \frac{\pi}{2N_1} - \boldsymbol{inv}\alpha_0 + \tan\left[\arccos\frac{N_1\cos\alpha_0}{\sqrt{(N_2+2)^2+(N_1+N_2)^2-2(N_2+2)(N_1+N_2)\cos(\arccos\frac{N_2\cos\alpha_0}{N_2+2}-\alpha_0)}}\right] \tag{2.51}$$

For the counterpart of $\alpha_{1,1}^{0}$, the angle $\alpha_{1,1}^{0'}$ (corresponding to the gear) can be expressed as:

$$\alpha_{1,1}^{0'} = \angle B_2O_2D = \angle B_2O_2A_2 - \angle A_2O_2D \tag{2.52}$$

where $\angle B_2O_2A_2$ and $\angle A_2O_2D$ can be calculated as:

$$\angle B_2O_2A_2 = \arccos\frac{R_{b2}}{R_{O2}} \tag{2.53}$$

$$\angle A_2O_2D = \alpha_2' - \angle A_4O_2A_2 = \alpha_2' - \boldsymbol{inv}\arccos\frac{R_{b2}}{R_{O2}} \tag{2.54}$$

Substitute $\angle B_2O_2A_2$ in Equation (2.53) and $\angle A_2O_2D$ in Equation (2.54) into Equation (2.52) to obtain (recall Equation (2.10) on page 21):

$$\alpha_{1,1}^{0'} = \tan\left(\arccos\frac{R_{b2}}{R_{O2}}\right) - \alpha_2' \tag{2.55}$$

Now, substitute Equations (2.3), (2.5) and (2.43) into Equation (2.55) and simplify. The result will be:

$$\alpha_{1,1}^{0'} = \tan\left(\arccos\frac{N_2\cos\alpha_0}{N_2+2}\right) - \frac{\pi}{2N_2} - \boldsymbol{inv}\alpha_0 \tag{2.56}$$

Equation (2.56) gives the calculation formula of the angle $\alpha_{1,1}'$ when the angular displacement of the gear is zero. When the angular displacement of the gear is θ_2 (in this time, the corresponding angular displacement of the pinion is θ_1) (as shown in Figure 2.2), the angle $\alpha_{1,1}'$ will be:

$$\begin{aligned}\alpha_{1,1}' &= \alpha_{1,1}^{0'} - \theta_2 \\ &= \tan\left(\arccos\frac{N_2\cos\alpha_0}{N_2+2}\right) - \frac{\pi}{2N_2} - \boldsymbol{inv}\alpha_0 - \theta_2\end{aligned} \tag{2.57}$$

Consider the relation between the angular displacements of the pinion and the gear, θ_1 and θ_2. The initial reference displacement point (point A_2 in Figure 2.2) is selected as the point where the double-tooth-pair mesh duration begins. The angular velocities of the pinion and the gear, ω_1 and ω_2, have the following relationship [1]:

$$\omega_2 = \frac{N_1}{N_2}\omega_1 \tag{2.58}$$

Thus, we can obtain:

$$\theta_2 = \frac{N_1}{N_2}\theta_1 \tag{2.59}$$

Substitute ω_2 in Equation (2.59) into Equation (2.57). The result will be:

$$\alpha'_{1,1} = \tan\left(\arccos\frac{N_2\cos\alpha_0}{N_2+2}\right) - \frac{\pi}{2N_2} - \boldsymbol{inv}\alpha_0 - \frac{N_1}{N_2}\theta_1 \tag{2.60}$$

Equations (2.51) and (2.60) give the calculation formulae of the angles $\alpha_{1,1}$ and $\alpha'_{1,1}$, respectively, which are for the first pair of meshing teeth. Similarly, for the second pair of meshing teeth, there are corresponding angles $\alpha_{1,2}$ and $\alpha'_{1,2}$ (refer to Figure 2.2). For the angle $\alpha_{1,2}$, the difference from the angle $\alpha_{1,1}$ is only the angle $2\pi/N_1$. Thus, it can be expressed as:

$$\alpha_{1,2} = \alpha_{1,1} + \frac{2\pi}{N_1} = \theta_1 + \frac{3\pi}{2N_1} - \boldsymbol{inv}\alpha_0 + \tan\left[\arccos\frac{N_1\cos\alpha_0}{\sqrt{(N_2+2)^2+(N_1+N_2)^2-2(N_2+2)(N_1+N_2)\cos(\arccos\frac{N_2\cos\alpha_0}{N_2+2}-\alpha_0)}}\right] \tag{2.61}$$

Correspondingly, the difference between the angles $\alpha'_{1,2}$ and $\alpha'_{1,1}$ is also only the angle $2\pi/N_2$, but the sign is negative, i.e. $-2\pi/N_2$. The expression is as

follows.

$$\begin{aligned} \alpha'_{1,2} &= \alpha'_{1,1} - \frac{2\pi}{N_2} \\ &= \tan\left(\arccos\frac{N_2\cos\alpha_0}{N_2+2}\right) - \frac{N_1}{N_2}\theta_1 - \frac{5\pi}{2N_2} - \boldsymbol{inv}\alpha_0 \end{aligned} \tag{2.62}$$

Now, we possess all the expressions for the angles $\alpha_{1,1}$, $\alpha'_{1,1}$, $\alpha_{1,2}$ and $\alpha'_{1,2}$, which will be used for the dynamic simulation in Chapter 4. Meanwhile, these expressions will be validated by the simulation results.

Within double-tooth-pair mesh duration, there are two pairs of teeth meshing at the same time. The effective stiffness of each pair can be calculated according to Equation (2.35) when i =1, 2, respectively. We assume that the total effective stiffness k_t is equal to the summation of these two pairs' stiffnesses $k_{t,1}$ and $k_{t,2}$. Then, k_t can be obtained by:

$$\begin{aligned} k_t &= k_{t,1} + k_{t,2} \\ &= \sum_{i=1}^{2} \frac{1}{\frac{1}{k_{h,i}} + \frac{1}{k_{b1,i}} + \frac{1}{k_{s1,i}} + \frac{1}{k_{a1,i}} + \frac{1}{k_{b2,i}} + \frac{1}{k_{s2,i}} + \frac{1}{k_{a2,i}}} \end{aligned} \tag{2.63}$$

For the single-tooth-pair meshing duration, the total effective mesh stiffness can be calculated according to Equation (2.34).

2.3.2 Double/Single-tooth-pair Meshing Duration

In this study, we define the angular displacement as the angle that the pinion/gear goes through from the initial reference point. Select point A_2 shown in Figure 2.2 as this reference point, which corresponds to the initial meshing point of the first pair of meshing teeth, i.e. the point where the double-tooth-pair meshing duration begins. Corresponding to this initial point A_2, the con-

tact point of the second pair mating teeth is point C. At this point, the angular displacements of the meshing gears, θ_1 and θ_2, are both zero. As the angular displacement increases, contact point will move from point C to point A_1. Correspondingly, point A_1' on the pinion will move to A_1. The angle $\angle A_1' O_1 A_1$ will be equal to the lasting angular displacement, which is defined as θ_d. Thus, during θ_d, there are always two pairs of teeth meshing simultaneously. After point A_1, the second pair of mating teeth will separate. The single-tooth-pair meshing duration begins. Until the angular displacement reaches $\theta_1 = 2\pi/N_1$, we are back to the situation similar to the zero-position. The corresponding angular displacement is defined as θ_s.

Refer to Figure 2.2. According to the geometry of the involute tooth profile, the angle θ_d is equal to $\angle A_1' O_1 A_1$, which can be calculated as:

$$\theta_d = \tan\left(\arccos\frac{N_1\cos\alpha_0}{N_1+2}\right) - \frac{2\pi}{N_1} - \tan\left[\arccos\frac{N_1\cos\alpha_0}{\sqrt{(N_2+2)^2+(N_1+N_2)^2-2(N_2+2)(N_1+N_2)\cos(\arccos\frac{N_2\cos\alpha_0}{N_2+2}-\alpha_0)}}\right] \quad (2.64)$$

Thus, based on Equation (2.64), when there are two tooth pairs meshing, the range of the angular displacement can be expressed as:

$$\theta_1 \in \left[(n-1)\frac{2\pi}{N_1},\quad \theta_d + (n-1)\frac{2\pi}{N_1}\right] \quad (n = 1,2,\cdots) \quad (2.65)$$

The lasting angle, θ_s, of the single-tooth-pair mesh duration within one mesh period is given by:

$$\theta_s = \frac{2\pi}{N_1} - \theta_d \quad (2.66)$$

The range of the angular displacement can be expressed as:

$$\theta_1 \in \left[(n-1)\frac{2\pi}{N_1} + \theta_d, \quad (n-1)\frac{2\pi}{N_1} + (\theta_d + \theta_s)\right] \quad (n = 1,2,\cdots) \tag{2.67}$$

2.3.3 Validation of the Derived Equations

Equations (2.64) and (2.66) can be validated by examining the *Contact Ratio*, which is a criterion of load distribution between the teeth being in mesh and applied to specify the average number of pairs of teeth in contact. There exist two definitions/descriptions for this term. One is "the ratio of the length of the working part of the action line to the base pitch" [3, 34]. The other is "the average number of pairs of teeth in contact according to the angular displacement" [3]. Both definitions are used by researchers to explain the physical meaning of the term *contact ratio*. The first one is in terms of the 'distance (line)' relation, and the second is in terms of the 'angular' relation. While the first is the more commonly used, the second is more useful in this study. This second definition formula may use the angles whose calculation formulae are derived and validated here. For a same term *contact ratio*, we use two definitions from two different angles (line/angular relation) . The second one is calculated by the equations (Equations (2.64) and (2.66)) to validate. Thus, if these two results are consistent, the equations derived are validated since we use the derived equations to obtain the second result.

Based on the former definition of contact ratio, it can be expressed as [3, 34]:

$$C_{r1} = \frac{\overline{A_1 A_2}}{p_b} \tag{2.68}$$

where p_b is the base circular pitch, which can be expressed as [3]:

$$p_b = p\cos\alpha_0 \tag{2.69}$$

where p is the circular pitch of mating gears, which is defined as:

$$p = \frac{\pi}{P} \tag{2.70}$$

where P is the diametral pitch of mating gears.

Substitute the parameters in Equations (2.1), (2.69), (2.4), (2.5) and (2.6) into Equation (2.68), the result is as follows [3, 34]:

$$C_{r1} = \frac{\sqrt{(N_1+2)^2-(N_1\cos\alpha_0)^2}+\sqrt{(N_2+2)^2-(N_2\cos\alpha_0)^2}-(N_1+N_2)\sin\alpha_0}{2\pi\cos\alpha_0} \tag{2.71}$$

Based on the latter description of contact ratio, we can calculate contact ratio as:

$$C_{r2} = \frac{\theta_s + 2\theta_d}{\frac{2\pi}{N_1}} = \frac{N_1}{2\pi}\left\{\tan\left(\arccos\frac{N_1\cos\alpha_0}{N_1+2}\right) - \tan\left[\arccos\frac{N_1\cos\alpha_0}{\sqrt{(N_2+2)^2+(N_1+N_2)^2-2(N_2+2)(N_1+N_2)\cos(\arccos\frac{N_2\cos\alpha_0}{N_2+2}-\alpha_0)}}\right]\right\} \tag{2.72}$$

To test correctness of Equations (2.64) and (2.66), we may compare the contact ratios calculated by the Equations (2.71) and (2.72), respectively. In our investigation, only gears without undercutting will be considered. (undercutting is a undesired case during gear manufacture, which makes the initial point of the involute curve not located on the base circle [3]. Under this condition, the meshing of gears will not be according to the involute profile during some meshing period. Undercutting will be present when the tooth number

of the pinion is relatively small.) In this case, the initial point of the involute profile belongs to the base circle. As shown in Figure 2.2, the distance between the initial mating point A_2 and the center of the pinion can not be less than the base radius in order to guarantee the contact is along the involute curve.

For convenience, we define the pressure angle to make the length of $\overline{A_2O_1}$ equal to the base radius as *critical pressure angle* α_{0b}. Given the numbers of teeth in a pair of meshing gears, α_{0b} can be obtained by solving Equation (2.73).

$$N_1 \cos\alpha_{0b} = \sqrt{(N_2+2)^2+(N_1+N_2)^2-2(N_2+2)(N_1+N_2)\cos(\arccos\frac{N_2\cos\alpha_{0b}}{N_2+2}-\alpha_{0b})} \tag{2.73}$$

Based on Equation (2.73), we can obtain critical pressure angles for different tooth numbers of mating gears as shown in Figure 2.4.

According to Equation (10.5.4) in [3], the minimal pressure angle without undercutting can be calculated by:

$$\alpha_{0m} = \arcsin\sqrt{\frac{2}{N_1}} \tag{2.74}$$

The minimal pressure angles without undercutting for different tooth numbers are shown in Figure 2.5. The difference (shown in Figure 2.6) between the minimal and critical pressure angles can be expressed as:

$$\Delta\alpha_0 = \alpha_{0m} - \alpha_{0b} \tag{2.75}$$

We find that the calculation results of *Contact Ratio* by Equations (2.71) and (2.72) are identical under the condition that pressure angle is greater than critical pressure angle α_{0b}. The following will investigate if this condition is

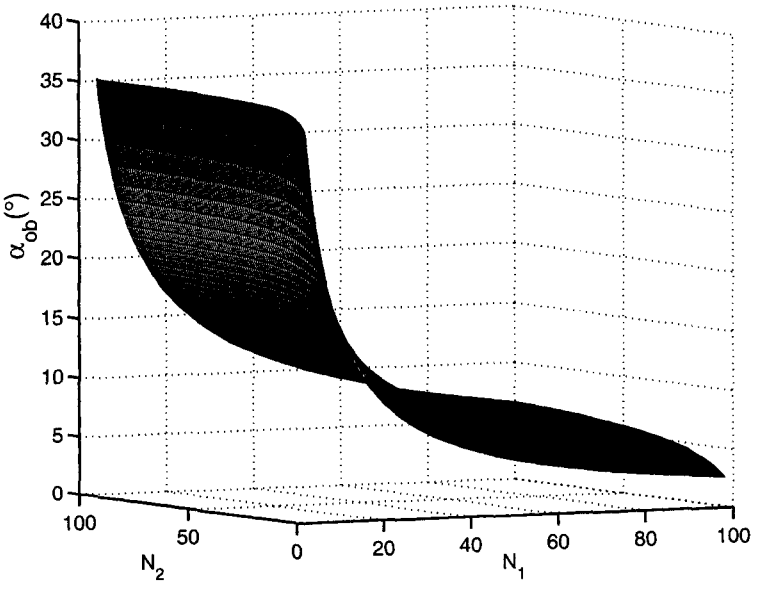

Figure 2.4: The critical pressure angle α_{ob} vs. the tooth numbers of the pinion and the gear N_1 & N_2

satisfied in this study.

From Figure 2.6, $\Delta\alpha_0$ is always greater than zero, i.e. the minimal pressure angle is always greater than the critical pressure angle. Therefore, in this study (for which no undercutting exists), the applied pressure angle greater than α_{0m} will be greater than α_{0b} as well. Thus, the results by Equations (2.71) and (2.72) are identical, which validates the correctness of Equations (2.64) and (2.66).

2.4 Relation of Mesh Stiffness and Angular Displacement

For a pair of steel gears with pressure angle 20°, tooth numbers 19/48, the diametral pitch $P = 8\ inch^{-1}$ and the width of teeth $L = 16\ mm$, the angular displacement of the pinion during one mesh period is 18.9° (=360°/N_1). The relations of stiffnesses and the angular displacement are shown in Figure 2.7.

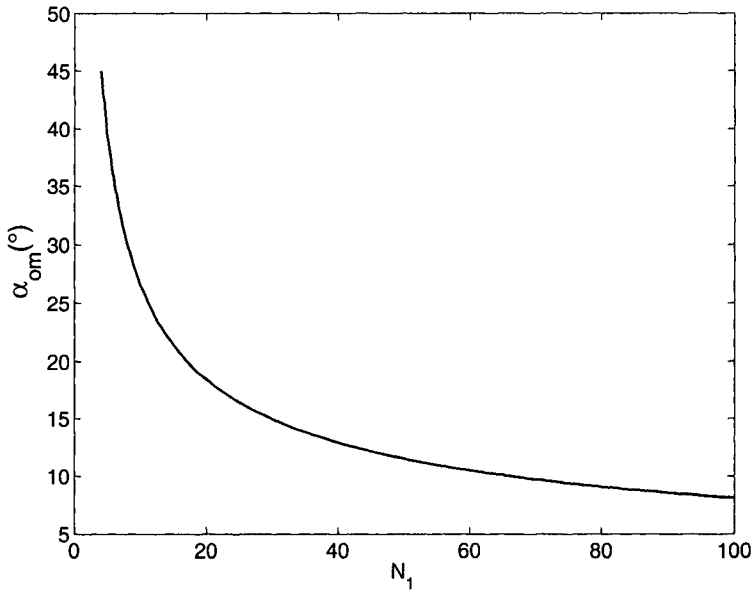

Figure 2.5: The minimal pressure angle α_{0m} for nonundercutting vs. the tooth number of the pinion N_1

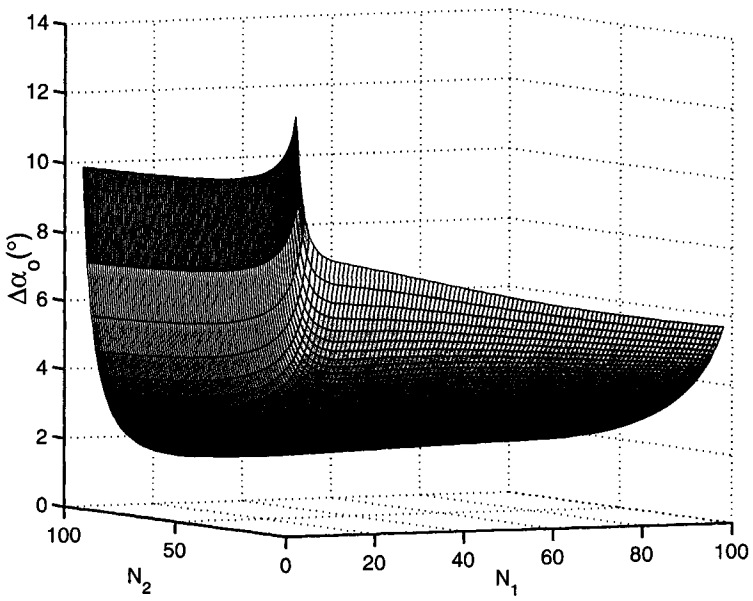

Figure 2.6: The difference $\Delta\alpha_0$ between the minimal and critical pressure angles vs. the tooth numbers of the pinion and the gear N_1 & N_2

In this figure, θ_1 is the angular displacement of the pinion. $\theta_1 = 0$ represents that a pair of teeth just begins mating (refer to point A_2 in Figure 2.2 on page 23).

Based on Equation (2.11) on page 24, the Hertzian stiffness k_h for each mating tooth pair is a constant, as shown in Figure 2.7(a).

For the first pair of meshing teeth, from Equation (2.38) on page 31, the axial compressive stiffness $k_{a1,1}$ of the pinion can be obtained as shown in Figure 2.7(b), where the peak line with very high value corresponds to the angular displacement $\theta_1 = 1.292°$, which corresponds to $\alpha_{1,1} = 0$ (refer to Figure 2.3 on page 26. $\alpha_{1,1}$ can be calculated by Equation (2.51) on page 33.). According to Equation (2.38), when $\alpha_{1,1} = 0$, the corresponding axial compressive stiffness value is infinity. Thus, according to Equation (2.35), in this position, the axial compressive stiffness has no contribution to the total effective mesh stiffness.

The shear stiffness $k_{s1,1}$ can be obtained by Equation (2.37) on page 31. The result is shown in Figure 2.7(c). The shear stiffness decreases as the angular displacement increases within a mesh period (a mesh period T_m corresponds to the angular displacement 18.9°.).

We can obtain the bending stiffness $k_{b1,1}$ by Equation (2.36) on page 31. The result is shown in Figure 2.7(d), where the peak point corresponds to the angular displacement $\theta_1 = 1.292°$ (corresponding to $\alpha_{1,1} = 0$).

For the mating tooth of the gear, one of the first pair of meshing teeth, axial compressive stiffness $k_{a2,1}$, shear stiffness $k_{s2,1}$ and bending stiffness $k_{b2,1}$ can be obtained by Equations (2.41), (2.40) and (2.39) on page 31, respectively. The results are shown in Figures 2.7(e), (f) and (g), respectively. It is observed that they increase as the angular displacement increases within a mesh period

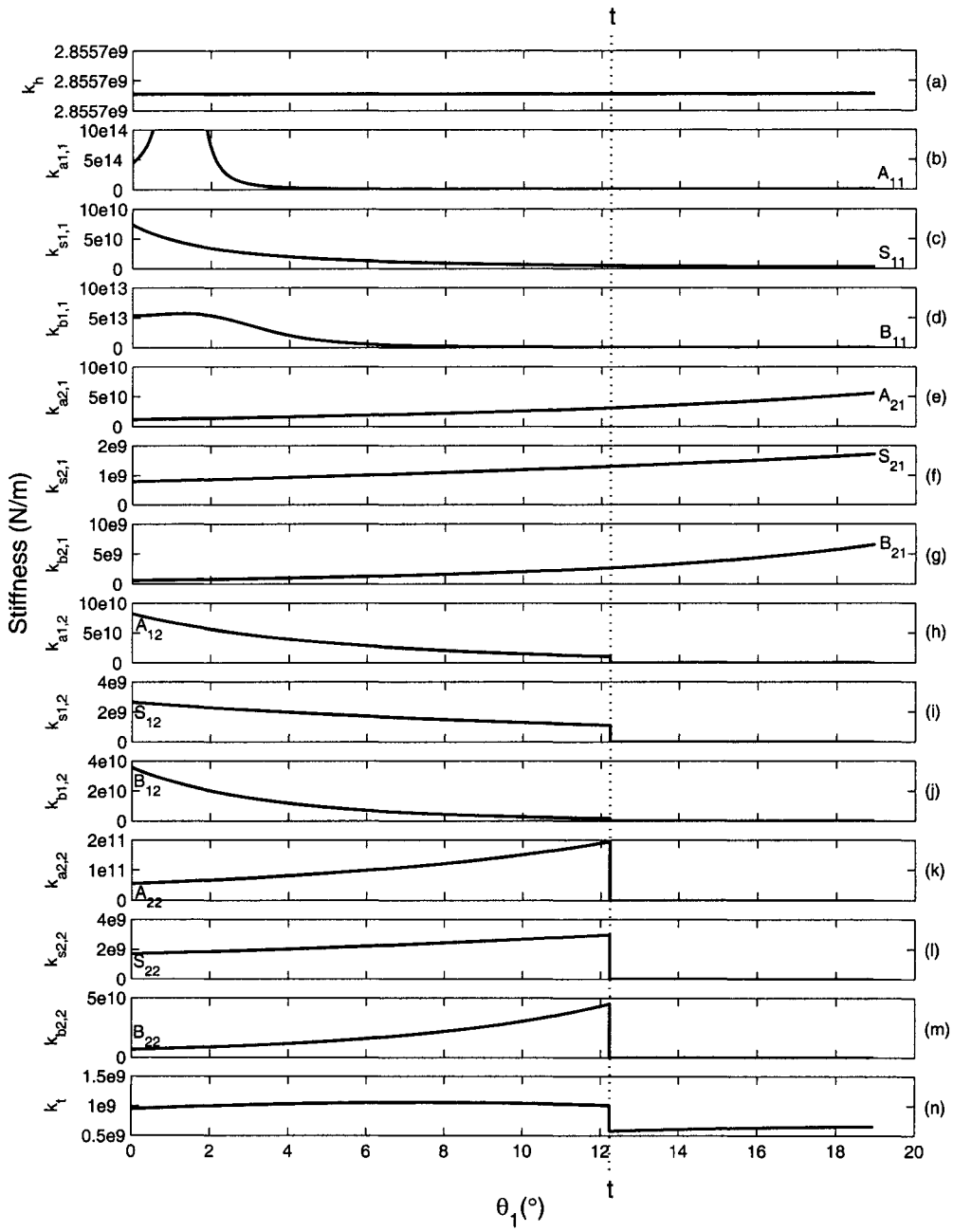

Figure 2.7: Stiffnesses vs. angular displacement θ_1 of the pinion: k_h-Hertzian stiffness; $k_{a1,1}/k_{a2,1}$-compressive stiffness of the pinion/gear tooth of the first pair; $k_{s1,1}/k_{s2,1}$- shear stiffness of the pinion/gear tooth of the first pair; $k_{b1,1}/k_{b2,1}$-bending stiffness of the pinion/gear tooth of the first pair; $k_{a1,2}/k_{a2,2}$-compressive stiffness of the pinion/gear tooth of the second pair; $k_{s1,2}/k_{s2,2}$-shear stiffness of the pinion/gear tooth of the second pair; $k_{b1,2}/k_{b2,2}$-bending stiffness of the pinion/gear tooth of the second pair; k_t-total mesh stiffness.

(a mesh period T_m corresponds to the angular displacement 18.9°.).

For the second pair of meshing teeth, the corresponding axial compressive stiffnesses ($k_{a1,2}$ and $k_{a2,2}$), shear stiffnesses ($k_{s1,2}$ and $k_{s2,2}$) and bending stiffnesses ($k_{b1,2}$ and $k_{b2,2}$) can be calculated by Equations (2.38), (2.41), (2.37), (2.40), (2.36) and (2.39), respectively. The results are shown in Figures 2.7(h-m), respectively. Different from those corresponding stiffnesses for the first pair of meshing teeth, there exists a common obvious discontinuous point for the second pair. After this point, all stiffnesses become zero. This point corresponds to the angular displacement $\theta_1 = 12.232°$, which represents the transition point from double-tooth-pair mesh to single-tooth-pair mesh, i.e. the second pair will end the mating at this point. The angles θ_d and θ_s of the double- and single-tooth-pair mesh durations within one mesh period can be calculated according to Equations (2.64) and (2.66) on page 37, respectively. They are $\theta_d = 12.232°$ and $\theta_s = 6.715°$, respectively.

In addition, in Figure 2.7, the values of stiffnesses at points A_{11}, S_{11}, B_{11}, A_{21}, S_{21} and B_{21} should be equal to those at points A_{12}, S_{12}, B_{12}, A_{22}, S_{22} and B_{22}, respectively. The reason is that beginning with point A_2 in Figure 2.2 on page 23, the mating point of the first pair will reach point C after one mesh period, where the stiffness values correspond to the values at points A_{11}, S_{11}, B_{11}, A_{21}, S_{21} and B_{21} in Figure 2.7. Point C, however, is exactly the initial mating point of the second pair, where the stiffness values correspond to the values at points A_{12}, S_{12}, B_{12}, A_{22}, S_{22} and B_{22} in Figure 2.7. Therefore, At the left side of the dotted line t-t, the first pair and the second pair will mesh simultaneously. After line t-t, only the first pair keeps meshing until the next mesh period.

All component stiffnesses have now been determined. By Equation (2.63)

on page 36 and Equation (2.34) on page 30, the total effective mesh stiffness with one mesh period can be obtained (as shown in Figure 2.7(n)). The mesh stiffness is changing with the angular displacement of the pinion. Within one mesh period, the value of mesh stiffness increases first. After reaching the peak point, it decreases until there is a discontinuous point, which corresponds to the transition point from double-tooth-pair mesh to single-tooth-pair mesh. After that point, the single-tooth-pair meshing duration begins, and thus the value of mesh stiffness increases again. Figure 2.8 gives the variation of the mesh stiffness within one shaft period, which comprises 19 mesh periods. It is observed that the mesh stiffness varies periodically. The period is the mesh period.

In comparison, if the shear stiffnesses are not considered in calculating the mesh stiffness, the total mesh stiffnesses for the double- and single-tooth-pair durations will be calculated according to Equation (2.63) getting rid of terms $k_{s1,i}$ and $k_{s2,i}$ on page 36 and Equation (2.34) getting rid of terms k_{s1} and k_{s2} on page 30, respectively. The result within one shaft period is shown in Figure 2.9. It is observed that the values of the total mesh stiffness are about two times higher than those with the shear stiffnesses considered. Therefore, the shear stiffness will affect the total effective mesh stiffness greatly.

To investigate the relations of bending, shear and axial compressive stiffnesses, the ratio plots are given in Figure 2.10. We see that the magnitudes of axial compressive and shear stiffnesses are close to and much smaller than those of the corresponding bending stiffnesses, respectively. Therefore, axial compressive and shear stiffnesses can not be ignored simply in calculating the total effective mesh stiffness.

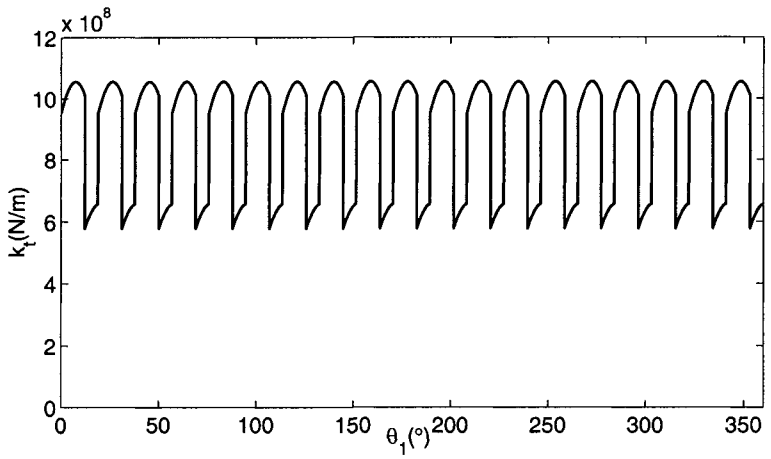

Figure 2.8: The total effective mesh stiffness k_t vs. the angular displacement θ_1 of the pinion within one shaft period T_1

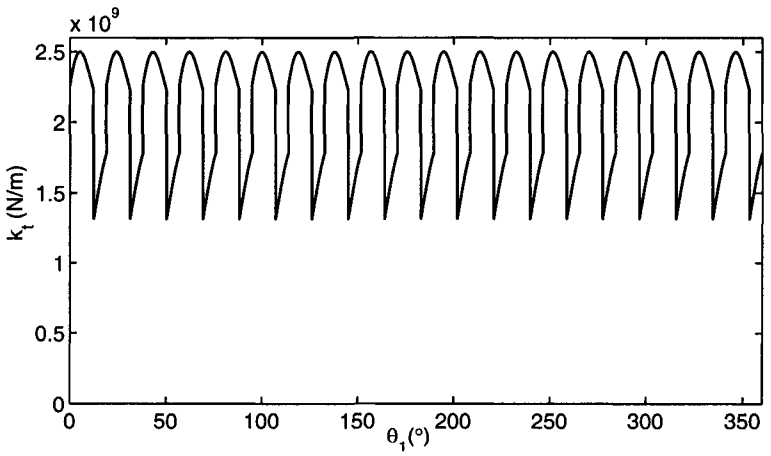

Figure 2.9: The total effective mesh stiffness k_t without the shear stiffness considered vs. the angular displacement θ_1 of the pinion within one shaft period T_1

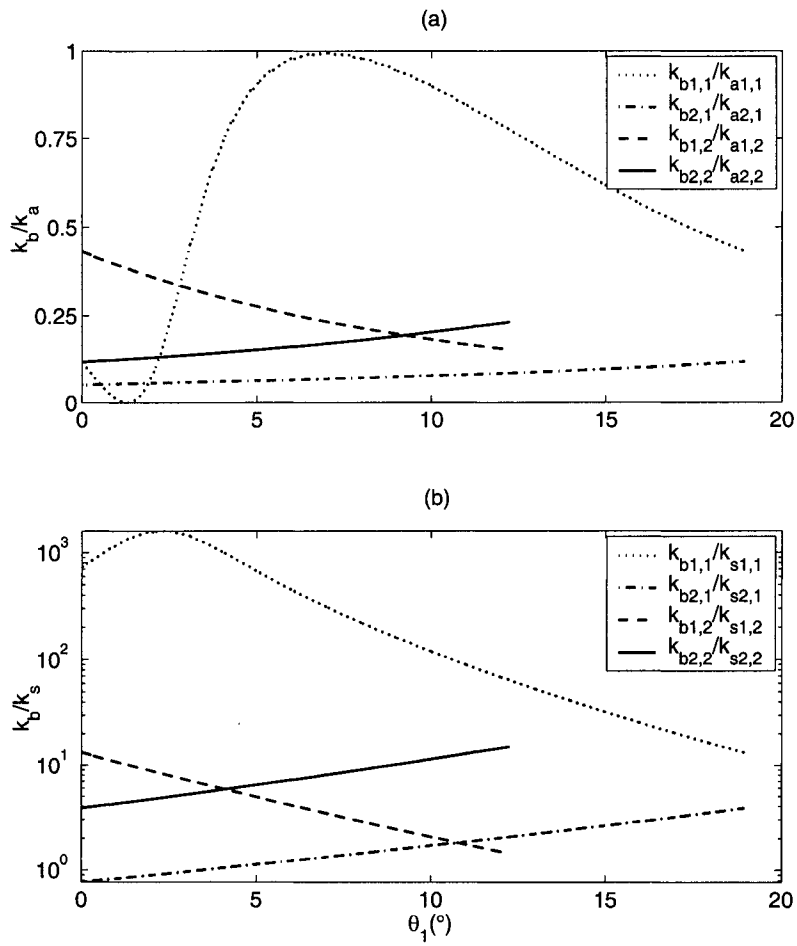

Figure 2.10: (a) Ratios of bending stiffnesses to axial compressive stiffnesses k_b/k_a vs. the angular displacement θ_1 of the pinion: $k_{b1,1}/k_{a1,1}$-ratio of the bending stiffness to axial compressive stiffness of the pinion tooth of the first mating pair; $k_{b2,1}/k_{a2,1}$-ratio of the bending stiffness to axial compressive stiffness of the gear tooth of the first mating pair; $k_{b1,2}/k_{a1,2}$-ratio of the bending stiffness to axial compressive stiffness of the pinion tooth of the second mating pair; $k_{b2,2}/k_{a2,2}$-ratio of the bending stiffness to axial compressive stiffness of the gear tooth of the second mating pair; (b) Ratios of bending stiffnesses to shear stiffnesses k_b/k_s vs. the angular displacement θ_1 of the pinion: $k_{b1,1}/k_{s1,1}$-ratio of the bending stiffness to shear stiffness of the pinion tooth of the first mating pair; $k_{b2,1}/k_{s2,1}$-ratio of the bending stiffness to shear stiffness of the gear tooth of the first mating pair; $k_{b1,2}/k_{s1,2}$-ratio of the bending stiffness to shear stiffness of the pinion tooth of the second mating pair; $k_{b2,2}/k_{s2,2}$-ratio of the bending stiffness to shear stiffness of the gear tooth of the second mating pair.

2.5 Summary

In this chapter, we derived the direct calculation formulae of mesh stiffness based on the potential energy method proposed by Yang and Lin [21]. The corresponding calculation formulae of parameters (such as $\alpha_{1,1}$, $\alpha'_{1,1}$, $\alpha_{1,2}$ and $\alpha'_{1,2}$) used for mesh stiffness calculation are derived. We developed the formulae for the calculation of the lasting angles of the double- and single-tooth-pair mesh durations within one mesh period as well, which are validated by parametric comparison (contact ratio).

The formulas derived in this chapter considered the shear stiffness, which was neglected by some previous studies. The results showed that the shear stiffness had a great influence upon the total mesh stiffness.

Based on the calculation formulae for the mesh stiffnesses of perfect gears in this chapter, we will discuss the mesh stiffnesses of gears with local tooth faults such as tooth chip, tooth crack and tooth breakage in next chapter.

Chapter 3

Introduction of Gear Local Faults

3.1 Introduction

In Chapter 2, for a pair of perfect mating gears with a contact ratio between 1 and 2, the direct calculation formulae of the total effective stiffness in each meshing duration (double-tooth-pair or single-tooth-pair) have been obtained by the potential energy method. By Equation (2.11) on page 24 and Equations (2.36-2.41) on pages 31-31, Hertzian, bending, shear and axial compressive stiffnesses can be calculated, respectively. Given gear material (Young's modulus E and Poisson's ratio ν are constants), the total effective mesh stiffness consisting of Hertzian, bending, shear and axial compressive stiffnesses depends on the geometry (shape and dimension) of the mating teeth of the gears investigated. Meanwhile, the localized gear faults are usually reflected in the changes of the tooth geometry. Therefore, these faults will cause the changes in the mesh stiffness of gears.

In this chapter, based on the calculation method of the mesh stiffness for perfect gears derived in Chapter 2, the mesh stiffnesses corresponding to three main localized gear faults such as tooth chip, tooth crack and tooth breakage will be investigated. For a pair of mating gears constructed of the same mate-

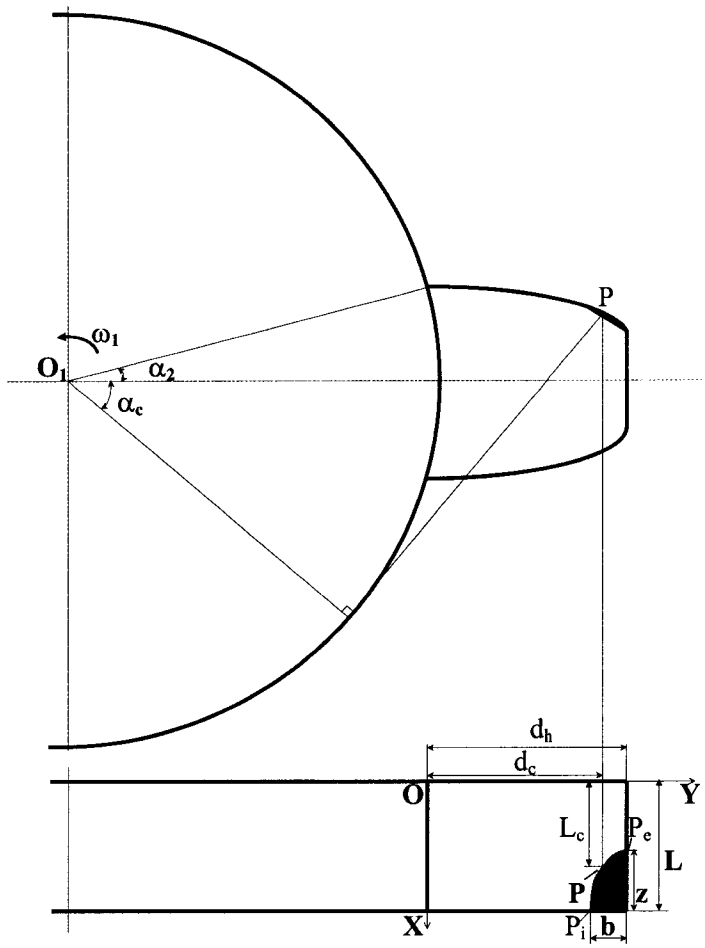

Figure 3.1: A chipped tooth

rial, the pinion usually gets worn first in that its rotation frequency is higher in comparison with that of the mating gear. Thus, only the faults in the pinion will be considered in this chapter.

3.2 Calculation of Mesh Stiffness of Pinion with a Chipped Tooth

Assume that there exists a chipped tooth in the pinion as shown in Figure 3.1, where the shade area is the chipped part. Assume that the chip is so thin compared with the thickness of the tooth, that the change of the tooth thick-

ness of the chipped part can be neglected when considering the bending, shear and axial compressive stiffnesses. Due to the integration effect of calculations of these three stiffnesses (refer to Equation (2.26) on page 28, Equation (2.30) and Equation (2.32) on page 29, respectively), the changes of these three stiffnesses caused by the chip can be neglected, i.e., the bending, shear and axial compressive stiffnesses in this case can be approximately considered the same as those in perfect case.

In addition, the torsional effect will be present as there exists a chipped tooth. This effect, however, has little to no contribution to the vibration response in the direction of the force F because the vibrations are not coupled to each other. Therefore, the torsional effect is negligible in this study.

Now, it is time to consider the Hertzian contact stiffness. According to Equation (2.11) on page 24, the Hertzian stiffness k_h is proportional to the width L of the tooth. For a perfect spur gear, the width along the tooth curve is constant. Therefore, the Hertzian stiffness will also remain unchanged. In the chipped case as shown in Figure 3.1, however, the width of the effective work surface will change as the contact position moves along the tooth curve. Correspondingly, the Hertzian stiffness will proportionally vary as well. It can be calculated as:

$$k_{h_{chip}} = \frac{\pi E L_c}{4(1-\nu^2)} \tag{3.1}$$

where L_c represents the width of the effective work surface. For the chip shape shown in Figure 3.1, the effective work width at the roof of this tooth has the minimal value $L-z$. Then, the width will increase along the tooth curve from the tooth roof toward the root. The width will change back to the normal width L at the position where the distance from the tooth roof is equal to b. Thereafter, the width will stay at the constant L. According to the XOY

plane rectangular coordinates as shown in the lower diagram of Figure 3.1, we assume that the curve $\widehat{P_iPP_e}$ of the chip profile is a segment of a hyperbolic curve. Given the coordinates of two end points $P_i(L, d_h{-}b)$ and $P_e(L{-}z, d_h)$, the relation between X and Y coordinates at some point P of this curve can be obtained according to the property of the hyperbolic curve. As a result, the width L_c of the effective work surface can be expressed as:

$$L_c = \begin{cases} L, & \text{if } 0{\leq}d_c{\leq}d_h{-}b \\ (\frac{d_h^2 z}{b} - d_h z)\frac{1}{d_c} + L - \frac{d_h z}{b}, & \text{if } d_h{-}b < d_c{\leq}d_h \end{cases} \tag{3.2}$$

where d_h is the tooth height (the distance between the roof and the root of the tooth). Referring to Equation (2.20) on page 27, d_c can be expressed as:

$$d_c = R_{b1}[(\alpha_c + \alpha_2)\sin\alpha_c + \cos\alpha_c - \cos\alpha_2] \tag{3.3}$$

where the angle α_c, (as shown in Figure 3.1, which corresponds to the angle α_1 in Figure 2.3 on page 26), uniquely determines the position of point P on the curve of this chipped tooth. The angle α_2 is half of the base tooth angle (as shown in Figure 3.1, which is the same as that in Figure 2.3).

From Equations (3.1-3.3), the Hertzian stiffness $k_{h_{chip}}$ will finally be a function of the angle α_c. Thus, when there exists a chipped tooth on the pinion, the total effective mesh stiffness can be expressed as:

$$k_{t_{chip}} = \frac{1}{\frac{1}{k_{h_{chip}}} + \frac{1}{k_{b1}} + \frac{1}{k_{s1}} + \frac{1}{k_{a1}} + \frac{1}{k_{b2}} + \frac{1}{k_{s2}} + \frac{1}{k_{a2}}} \tag{3.4}$$

In this study, the size of the chip is $z = 8\,mm$, $b = 2\,mm$ (as shown in Figure 3.1). For these parameters, the effective work contact width L_c of

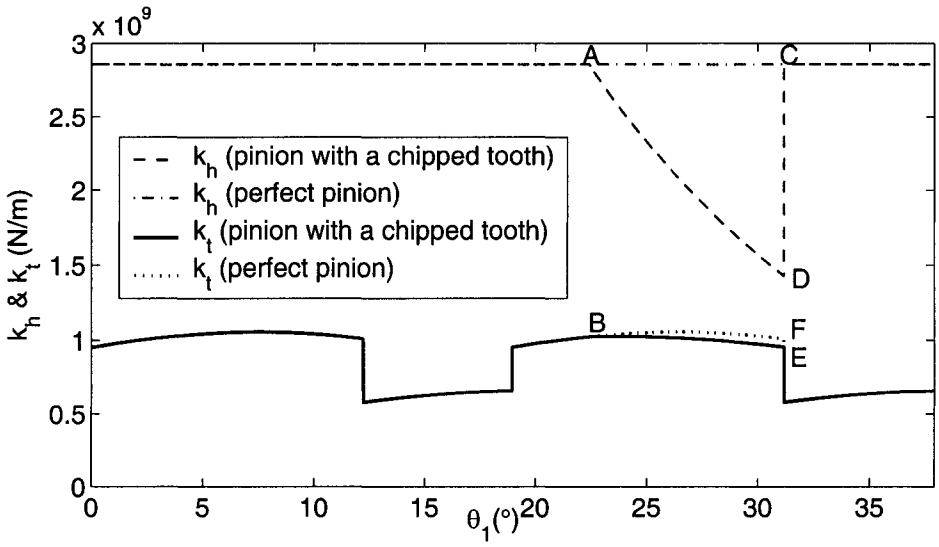

Figure 3.2: The Hertzian contact stiffness k_h and the total mesh stiffness k_t vs. the angular displacement θ_1 for the pinion with a chipped tooth

the mating teeth can be obtained according to Equation (3.2). The Hertzian contact stiffness can be calculated by Equation (3.1). The result is shown in Figure 3.2. Point A corresponds to the initial contact position of the chipped part, which corresponds to the angular displacement of the pinion $\theta_1 = 22.4°$. From point A to point D, the Hertzian stiffness decreases with the decrease of the effective contact width L_c. Point D correspond to the transition point from double-tooth-pair mesh to single-tooth-pair mesh. The corresponding variation of the total effective mesh stiffness is also shown in this figure. Instead of curve $\widehat{BF}$, the mesh stiffness will change as $\widehat{BE}$ during teeth mating in the chipped part, which reflects the shape of the chipped part and validates the derived expressions for the calculation of the total mesh stiffness.

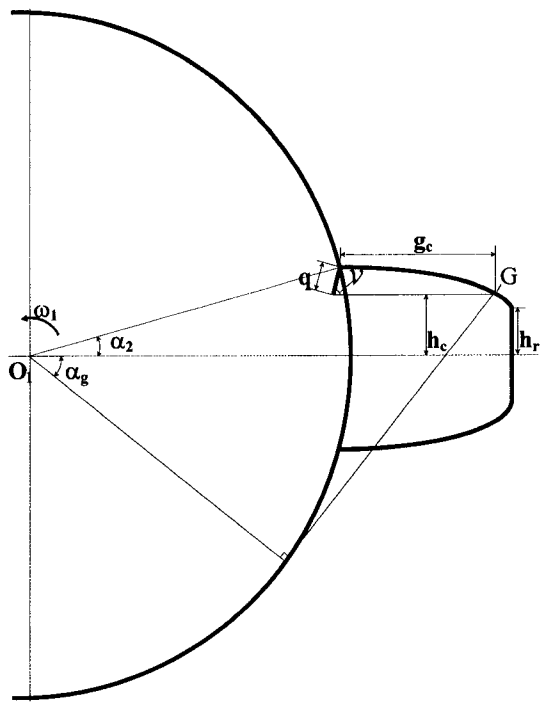

Figure 3.3: A cracked tooth

3.3 Calculation of Mesh Stiffness of Pinion with a Cracked Tooth

Assume that there exists a crack at the root of the pinion and the depth of the crack is a constant q along the width of the tooth. It is also assumed that the tooth with this crack is still considered as a cantilevered beam. The boundary condition is that the root of this tooth does not experience any deflection.

In this study, we will only consider the case when q is less than half of the base chordal tooth thickness (refer to Figure 2.1 on page 19 for the nomenclature). This case corresponds to the relatively shallow crack in the tooth, which is the most common cracked case in the real world since the tooth will rapidly break when there exists a deep crack (more than half of the base chordal tooth thickness). The intersection angle ν between the crack and the central line of the tooth is also a constant (as shown in Figure 3.3). The curve of the tooth

profile remains perfect. In this case, based on Equation (2.11) on page 24, the Hertzian contact stiffness will still be a constant since the work surface of the tooth has no defect and the width of the effective work surface will always be a constant L. For the axial compressive stiffness, it will be considered the same with that under the perfect condition in that the crack part can still bear the axial compressive force as if no crack exists. Therefore, with a tooth crack, Hertzian and axial compressive stiffnesses can still be calculated according to Equation (2.11) on page 24 and Equation (2.32) on page 29, respectively.

The bending and shear stiffnesses, however, will change due to the influence of the crack. Referring to both Figure 2.3 on page 26, which shows the definitions of some symbols used in Equation (3.5) and Equation (3.6), and Figure 3.3, when the crack is present, the effective area moment of inertia and area of the cross section at a distance of x from the tooth root will be calculated as Equation (3.5) (instead of I_x in Equation (2.22) on page 27) and Equation (3.6) (instead of A_x in Equation (2.29) on page 28), respectively.

$$I_{xc} = \begin{cases} \frac{1}{12}(h_c + h_x)^3 L, & \text{if } x \leq g_c \\ \frac{1}{12}(2h_x)^3 L = \frac{2}{3}h_x^3 L, & \text{if } x > g_c \end{cases} \tag{3.5}$$

$$A_{xc} = \begin{cases} (h_c + h_x)L, & \text{if } x \leq g_c \\ 2h_x L, & \text{if } x > g_c \end{cases} \tag{3.6}$$

where h_x can be obtained by Equation (2.23) on page 27, and h_c is the distance from the root of the crack to the central line of the tooth, which corresponds to point G on the tooth profile and the angle α_g (as shown in Figure 3.3). h_c

can be calculated by (based on Figure 2.3 and Figure 3.3):

$$h_c = R_{b1}\sin\alpha_2 - q\sin v \tag{3.7}$$

Following the similar procedure for deriving Equation (2.26) in section 2.2.2, the corresponding formulae of the bending and shear stiffnesses under the cracked condition can be derived as follows according to different cases.

a. *When* $h_c < h_r$ or *when* $h_c \geq h_r$ & $\alpha_1 \leq \alpha_g$

As shown in Figure 3.3, h_r is half of the roof chordal tooth thickness (refer to Figure 2.1 on page 19 for the nomenclature). In this case, x shown in Figure 2.3 on page 26 is always less than or equal to g_c shown in Figure 3.3. Thus, I_{xc} and A_{xc} should be calculated by the upper ones of Equation (3.5) and Equation A_{xc}, respectively. Substitute h_c in Equation (3.7) and h_x in Equation (2.23) on page 27 into Equation (3.5) and Equation (3.6). The results are as follows.

$$I_{xc} = \frac{1}{12}\{R_{b1}[\sin\alpha_2 + (\alpha+\alpha_2)\cos\alpha - \sin\alpha] - q\sin v\}^3 L \tag{3.8}$$

$$A_{xc} = \{R_{b1}[\sin\alpha_2 + (\alpha+\alpha_2)\cos\alpha - \sin\alpha] - q\sin v\}L \tag{3.9}$$

Now, replace I_x in Equation (2.21) on page 27 and A_x in Equation (2.27) on page 28 by I_{xc} and A_{xc}, respectively. Equation (2.21) will become:

$$U_b = \int_0^d \frac{[F_b(d-x) - M]^2}{2EI_{xc}}dx \tag{3.10}$$

Equation (2.21) will become:

$$U_s = \int_0^d \frac{1.2{F_b}^2}{2GA_{xc}}dx \tag{3.11}$$

Substitute U_b in Equation (2.13) on page 24 into the left side of Equation (3.10), and substitute F_b, M, d, I_{xc}, x, and dx in Equations (2.16), (2.18), (2.20), (3.8), (2.24) and (2.25) into the right side of Equation (3.10). After simplification, the result will be:

$$\frac{1}{k_{b_{crack}}} = \int_{-\alpha_1}^{\alpha_2} \frac{12\{1+\cos\alpha_1[(\alpha_2-\alpha)\sin\alpha-\cos\alpha]\}^2(\alpha_2-\alpha)\cos\alpha}{EL[\sin\alpha_2-\frac{q}{R_{b1}}\sin v+\sin\alpha+(\alpha_2-\alpha)\cos\alpha]^3}d\alpha \quad (3.12)$$

Substitute U_s in Equation (2.14) on page 25 into the left side of Equation (3.11), and substitute F_b, A_{xc}, x, and dx in Equations (2.16), (3.9), (2.24) and (2.25) into the right side of Equation (3.11). After simplification, the result will be:

$$\frac{1}{k_{s_{crack}}} = \int_{-\alpha_1}^{\alpha_2} \frac{2.4(1+\nu)(\alpha_2-\alpha)\cos\alpha\cos^2\alpha_1}{EL[\sin\alpha_2-\frac{q}{R_{b1}}\sin v+\sin\alpha+(\alpha_2-\alpha)\cos\alpha]}d\alpha \quad (3.13)$$

b. *When* $h_c \geq h_r$ & $\alpha_1 > \alpha_g$

In this case, the contact point of a pair of mating gears on the tooth profile will be located between point G and the tooth roof (refer to Figure 2.3 on page 26 and Figure 3.3). Thus, there exist two cases for calculations of I_{xc} and A_{xc}, $x \leq g_c$ (corresponding to $\alpha \leq \alpha_g$) and $x > g_c$ (corresponding to $\alpha > \alpha_g$), as shown in Equation (3.5) and Equation (3.6), respectively. The whole integrations for calculations of k_b and k_s will consist of two parts, respectively. The first part, corresponding to $\alpha \leq \alpha_g$, can be calculated referring to Equation (3.10) and Equation (3.11), respectively. The lower and upper limits of the integration variable α are $-\alpha_g$ and α_2, respectively. The second part, corresponding to $\alpha > \alpha_g$, can be obtained referring to Equations (2.21) and (2.27) with the lower limit $-\alpha_1$ and the upper limit $-\alpha_g$. Therefore, the bending and

shear stiffnesses will be equal to the summation of these two parts as follows.

$$\frac{1}{k_{b_{crack}}} = \int_{-\alpha_g}^{\alpha_2} \frac{12\{1+\cos\alpha_1[(\alpha_2-\alpha)\sin\alpha-\cos\alpha]\}^2(\alpha_2-\alpha)\cos\alpha}{EL[\sin\alpha_2-\frac{q}{R_{b1}}\sin v+\sin\alpha+(\alpha_2-\alpha)\cos\alpha]^3}d\alpha$$
$$+\int_{-\alpha_1}^{-\alpha_g} \frac{3\{1+\cos\alpha_1[(\alpha_2-\alpha)\sin\alpha-\cos\alpha]\}^2(\alpha_2-\alpha)\cos\alpha}{2EL[\sin\alpha+(\alpha_2-\alpha)\cos\alpha]^3}d\alpha \quad (3.14)$$

$$\frac{1}{k_{s_{crack}}} = \int_{-\alpha_g}^{\alpha_2} \frac{2.4(1+\nu)(\alpha_2-\alpha)\cos\alpha\cos^2\alpha_1}{EL[\sin\alpha_2-\frac{q}{R_{b1}}\sin v+\sin\alpha+(\alpha_2-\alpha)\cos\alpha]}d\alpha$$
$$+\int_{-\alpha_1}^{-\alpha_g} \frac{1.2(1+\nu)(\alpha_2-\alpha)\cos\alpha\cos^2\alpha_1}{EL[\sin\alpha+(\alpha_2-\alpha)\cos\alpha]}d\alpha \quad (3.15)$$

Thus, when there exists a cracked tooth on the pinion, the total effective mesh stiffness can be expressed as:

$$k_{t_{crack}} = \frac{1}{\frac{1}{k_h}+\frac{1}{k_{b_{crack}}}+\frac{1}{k_{s_{crack}}}+\frac{1}{k_{a1}}+\frac{1}{k_{b2}}+\frac{1}{k_{s2}}+\frac{1}{k_{a2}}} \quad (3.16)$$

Consider a crack at the root of the pinion with the depth $q = 3.1mm$ and the angle $\nu = 45°$ (as shown in Figure 3.3). In this case, the Hertzian and axial compressive stiffnesses can still be calculated according to Equation (2.11) on page 24 and Equation (2.32) on page 29, respectively.

The bending and shear stiffnesses, however, will change due to the influence of the crack (shown in Figure 3.4), which can be obtained by Equations (3.12), (3.14), (3.13) and (3.15). The corresponding total mesh stiffness $k_{t_{crack}}$ can be calculated by Equation (3.16). The result is shown in Figure 3.5.

From Figure 3.4, it is observed that the bending and shear stiffnesses greatly decrease due to the existence of the crack. The influences spread over the mating duration of this cracked tooth, which corresponds to the angular displacement θ_1 from zero to 31.2°, i.e. one mesh period plus the duration of double-tooth-pair mesh. The total mesh stiffness decreases appreciably due

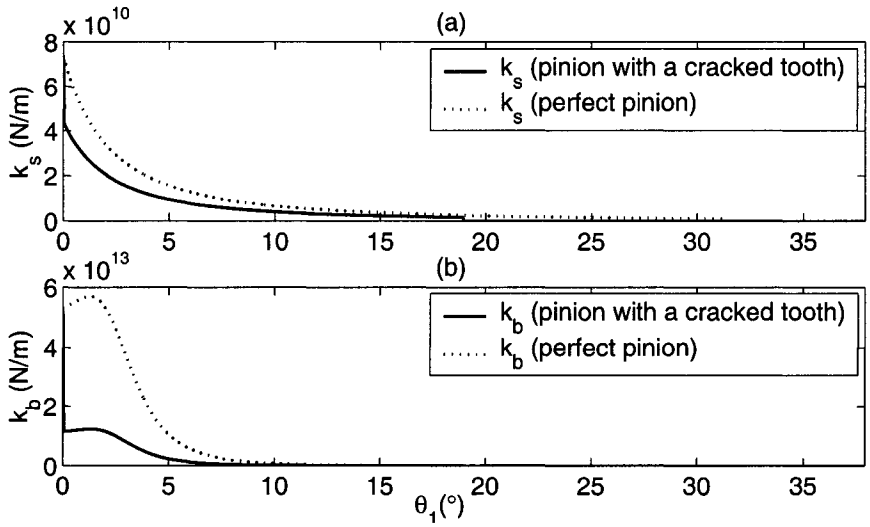

Figure 3.4: (a) The shear stiffness k_s vs. the angular displacement θ_1 for the pinion with a cracked tooth; (b) The bending stiffness k_b vs. the angular displacement θ_1 for the pinion with a cracked tooth

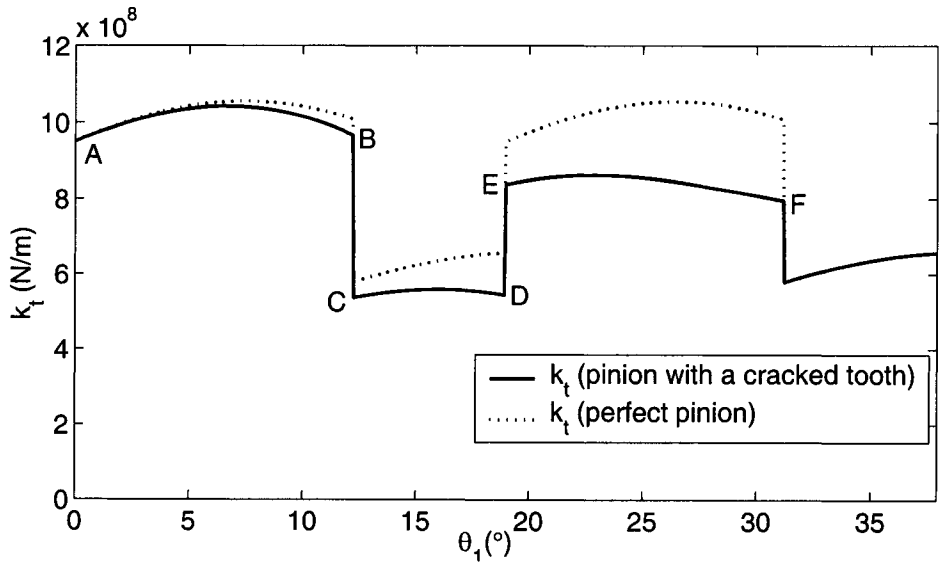

Figure 3.5: The total mesh stiffness k_t vs. the angular displacement θ_1 for the pinion with a cracked tooth

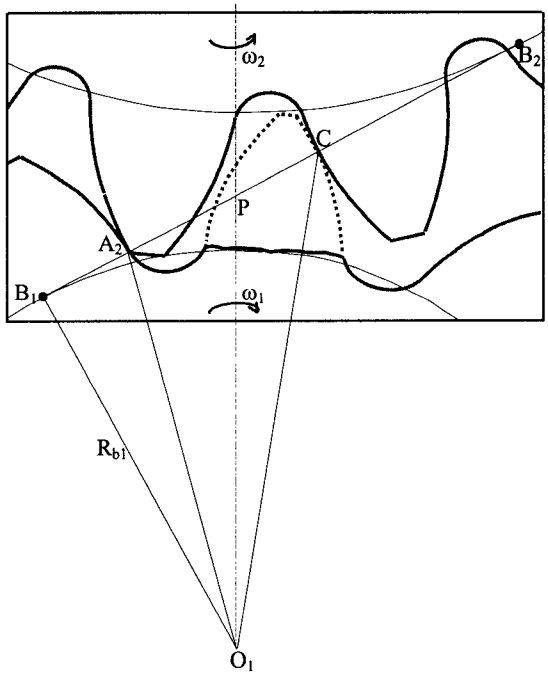

Figure 3.6: A broken tooth

to the crack within the double-tooth-pair mesh duration (curve $\widehat{AB}$ in Figure 3.5). From point C to point D and point E to point F, the total mesh stiffness decreases significantly. The result reflects the influence of the crack on the mesh stiffness and validates the derived expressions for the calculation of the total mesh stiffness.

3.4 Calculation of Mesh Stiffness of Pinion with a Broken Tooth

In the previous two sections, the calculation methods of mesh stiffnesses of the pinion with chipped and cracked defects have been investigated, respectively. In this section, we will focus on the mesh stiffness calculation under tooth-broken condition.

Assume that one of the teeth on the pinion is broken as shown in Figure

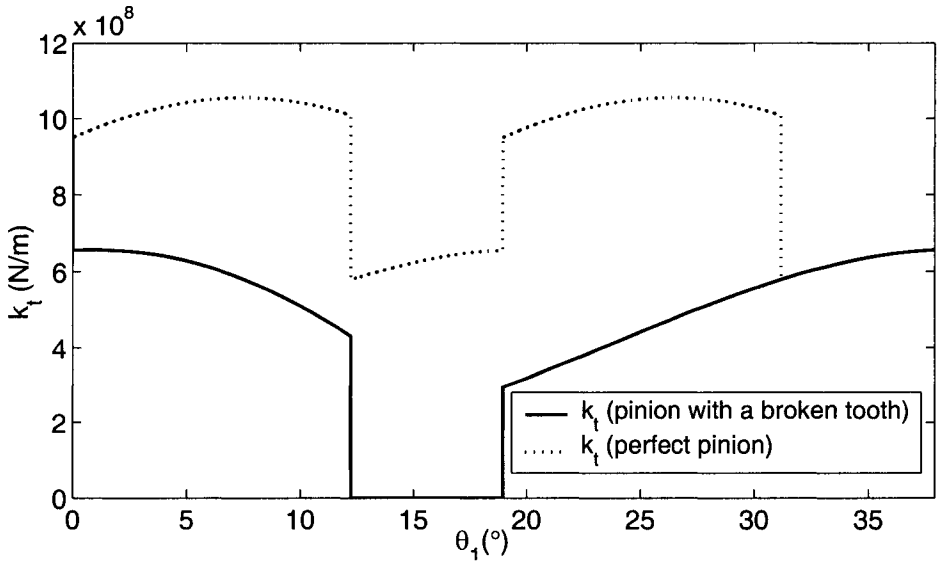

Figure 3.7: The total mesh stiffness k_t vs. the angular displacement θ_1 for the pinion with a broken tooth

3.6. The dotted-line tooth represents the missing one. If this tooth were not broken, it would become meshed with a tooth of the mating gear when it rotates to the engagement area. Within the double-tooth-pair duration, there are two pairs of teeth meshing at the same time. Only one pair of teeth are meshing during the single-tooth-pair duration. However, with dotted-line tooth missing, in comparison with the perfect case, there will be only one pair meshing during original double-tooth-pair duration since the tooth will lose contact at the position of the missing tooth. Thus, the total effective mesh stiffness will only consist of the mesh stiffness of one pair of teeth. Instead of Equation (2.63) on page 36 in section 2.3, the total effective mesh stiffness will become:

$$k_{t_{broken}} = \frac{1}{\frac{1}{k_{h,1}} + \frac{1}{k_{b1,1}} + \frac{1}{k_{s1,1}} + \frac{1}{k_{a1,1}} + \frac{1}{k_{b2,1}} + \frac{1}{k_{s2,1}} + \frac{1}{k_{a2,1}}} \tag{3.17}$$

Correspondingly, during original single-tooth-pair duration, the total effective mesh stiffness will become zero as a result of no tooth mesh. In this case, it is assumed that the driven gear can still continue rotating during this short term due to the rotation inertia. Thus, the corresponding mesh stiffness is shown in Figure 3.7. The mesh stiffness is much lower than that in the perfect case.

3.5 Summary

In this chapter, based on the perfect case discussed in Chapter 2, we derived the expressions of the effective mesh stiffness of the mating gears with three kinds of localized tooth faults such as chipped, cracked and broken tooth, respectively. These expressions will be validated by the simulation results in Chapter 4.

With the help of these expressions, the corresponding gear faults can be introduced to investigate their influence on vibration response of gear system, which will be discussed in the following chapter.

Chapter 4

Dynamic Simulation of System Response of Gearbox

4.1 Introduction

In the foregoing chapters, we derived the expressions for the mesh stiffnesses of perfect gears and gears with local tooth faults such as tooth chip, tooth crack and tooth breakage. As an important parameter of gear dynamics, mesh stiffness can be used to represent different tooth faults of gears as shown in Chapter 3. With the help of these derived expressions, we can investigate the influence of mesh stiffness variation due to some tooth fault on vibration response of a gear system.

In this chapter, a one-stage gear dynamic model considering the time-varying mesh stiffness and lateral and torsional vibrations will be simulated to study the effects of three kinds of local tooth faults. By analytical and/or numerical methods, vibration acceleration responses under different gear conditions will be investigated. The simulation results in this chapter will also be used to validate the expressions derived in Chapter 2 and Chapter 3.

On the basis of the one-stage gear dynamic model, analytical solutions of

motion equations of a gear system will be obtained for the vibration response in the direction parallel to teeth in mesh (the x direction). Numerical solutions will be obtained for the vibration response in the direction vertical to teeth in mesh (the y direction). Simulation data between normal and fault cases will be compared under different fault conditions.

4.2 Model of Gear Dynamics

In Chapter 1, we briefly described models of gear dynamics used by other researchers. Among these models, a dynamic model coupling both torsional and lateral motions is ideal for investigating the vibration response properties of the gear system, especially for the study on the response of gearbox casing. The reason is that one typically considers measuring the lateral vibration accelerations by mounting sensors close to the bearings on the gearbox casing. For simplification, we assume that the gearbox casing is rigid so that the vibration propagation along the casing is linear. Thus, the vibration response properties of gears in lateral directions are consistent with those on the gearbox casing.

Figure 4.1 shows the model to be used in our study. The definitions of some symbols are shown on page 68. It is a one-stage mass-spring-damper 8-DOF involute spur gear dynamic model with both torsional and lateral vibration considered, which was developed by Bartelmus [19]. In their study, two constant mesh stiffnesses were used for single- and double-tooth-pair mating durations, respectively. In our investigation however, we will consider time-varying mesh stiffness for each duration. The calculation expressions of mesh stiffness for three cases of local tooth faults were derived in Chapter 3.

The system is driven by electric motor with a torque M_1, and loaded with torque M_2. The motor shaft and the shaft that the pinion mounts on are

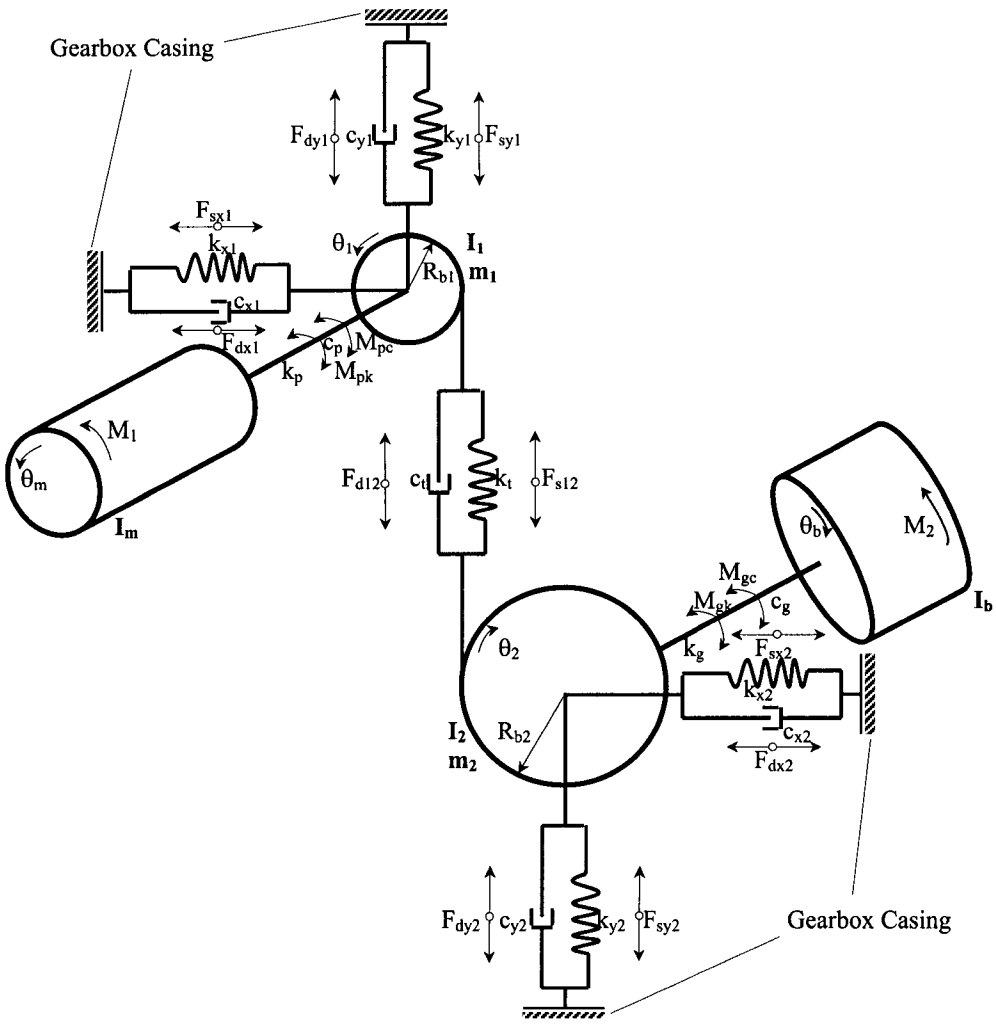

Figure 4.1: A model of one-stage gearbox dynamics: F_{dy1}, F_{dx1}, F_{dy2} and F_{dx2} - the damping forces of the bearings; F_{sy1}, F_{sx1}, F_{sy2} and F_{sx2} - the stiffness forces of the bearings; F_{d12} and F_{s12} - the stiffness and damping inter-tooth forces; M_{pk} and M_{gk} - the stiffness moments of the couplings; M_{pc} and M_{gc} - the damping moments of the couplings. The definitions of other symbols are shown on page 68.

coupled with a flexible coupling named "input coupling". The similar style coupling named "output coupling" is applied to couple the shaft of the load and the shaft that the gear mounts on. The shafts, upon which the pinion and the gear are mounted, are supported by bearings. The bearings are attached to the gearbox casing. In Figure 4.1, the four shadowed parts represent the gearbox casing, which is considered as the rigid casing for simplification. The equations of motion for the system shown may be described as follows [19]:

Consider the motion in the x direction. The motion equations are:

$$m_1\ddot{x}_1 = -k_{x_1}x_1 - c_{x_1}\dot{x}_1 \tag{4.1}$$

$$m_2\ddot{x}_2 = -k_{x_2}x_2 - c_{x_2}\dot{x}_2 \tag{4.2}$$

Now examine the motion in the y direction. The motion equations are:

$$m_1\ddot{y}_1 = -k_{y_1}y_1 - c_{y_1}\dot{y}_1 + k_t(R_{b1}\theta_1 - R_{b2}\theta_2 - y_1 + y_2) + c_t(R_{b1}\dot{\theta}_1 - R_{b2}\dot{\theta}_2 - \dot{y}_1 + \dot{y}_2) \tag{4.3}$$

$$m_2\ddot{y}_2 = -k_{y_2}y_2 - c_{y_2}\dot{y}_2 + k_t(R_{b1}\theta_1 - R_{b2}\theta_2 - y_1 + y_2) + c_t(R_{b1}\dot{\theta}_1 - R_{b2}\dot{\theta}_2 - \dot{y}_1 + \dot{y}_2) \tag{4.4}$$

For the rotary motions of the pinion and the gear, the motion equations will be:

$$\begin{aligned} I_1\ddot{\theta}_1 = {} & k_p(\theta_m - \theta_1) + c_p(\dot{\theta}_m - \dot{\theta}_1) - R_{b1}[k_t(R_{b1}\theta_1 - R_{b2}\theta_2 \\ & - y_1 + y_2) + c_t(R_{b1}\dot{\theta}_1 - R_{b2}\dot{\theta}_2 - \dot{y}_1 + \dot{y}_2)] \end{aligned} \tag{4.5}$$

$$\begin{aligned} I_2\ddot{\theta}_2 = {} & -k_g(\theta_2 - \theta_b) - c_g(\dot{\theta}_2 - \dot{\theta}_b) + R_{b2}[k_t(R_{b1}\theta_1 - R_{b2}\theta_2 \\ & - y_1 + y_2) + c_t(R_{b1}\dot{\theta}_1 - R_{b2}\dot{\theta}_2 - \dot{y}_1 + \dot{y}_2)] \end{aligned} \tag{4.6}$$

For the rotary motions of the motor and the load, the motion equations can be expressed as:

$$I_m\ddot{\theta}_m = M_1 - k_p(\theta_m - \theta_1) - c_p(\dot{\theta}_m - \dot{\theta}_1) \tag{4.7}$$

$$I_b\ddot{\theta}_b = -M_2 + k_g(\theta_2 - \theta_b) + c_g(\dot{\theta}_2 - \dot{\theta}_b) \tag{4.8}$$

where:

I_m - mass moment of inertia of the motor;

I_b - mass moment of inertia of the load;

I_1 - mass moment of inertia of the pinion;

I_2 - mass moment of inertia of the gear;

M_1- input motor torque;

M_2 - output torque from load;

m_1 - mass of the pinion;

m_2 - mass of the gear;

R_{b1} - base circle radius of pinion;

R_{b2} - base circle radius of gear;

k_p - torsional stiffness of the input flexible coupling

k_g - torsional stiffness of the output flexible coupling

c_p - damping coefficient of the input flexible coupling;

c_g - damping coefficient of the output flexible coupling;

k_{x_1} - horizontal radial stiffness of the input bearings;

k_{x_2} - horizontal radial stiffness of the output bearings;

k_{y_1} - vertical radial stiffness of the input bearings;

k_{y_2} - vertical radial stiffness of the output bearings;

c_{x_1} - horizontal radial viscous damping coefficient of the input bearings;

c_{x_2} - horizontal radial damping coefficient of the output bearings;

c_{y_1} - vertical radial damping coefficient of the input bearings;

c_{y_2} - vertical radial damping coefficient of the output bearings;

k_t - mesh stiffness;

c_t - mesh damping coefficient;

x_1 - linear displacement of pinion in the direction parallel to teeth in mesh (the x direction);

x_2 - linear displacement of gear in the x direction;

y_1 - linear displacement of pinion in the direction vertical to teeth in mesh (the y direction);

y_2 - linear displacement of gear in the y direction;

θ_m - angular displacement of motor;

θ_1 - angular displacement of pinion;

θ_2 - angular displacement of gear;

θ_b - angular displacement of load;

The symbols with one and two overdot, say $\dot{x}$ *and* $\ddot{x}$, represent velocities and accelerations, respectively.

To make equations more compact, Equations (4.1)-(4.8) can be rewritten as:

$$\mathbf{m}\ddot{\mathbf{x}} + \mathbf{C}_x\dot{\mathbf{x}} + \mathbf{K}_x\mathbf{x} = 0 \tag{4.9}$$

$$\mathbf{m}\ddot{\mathbf{y}} + \mathbf{C}_y\dot{\mathbf{y}} + \mathbf{K}_y\mathbf{y} = \mathbf{C}_t\mathbf{R}\dot{\theta}_{12} + \mathbf{K}_t\mathbf{R}\theta_{12} \tag{4.10}$$

$$\mathbf{I}_{12}\ddot{\Theta}_d + \mathbf{C}_z\dot{\Theta}_d + \mathbf{K}_z\Theta_d = \mathbf{C}_{pg}\dot{\Theta}_{mb} + \mathbf{K}_{pg}\Theta_{mb} + \mathbf{R}^T\mathbf{C}_t^T\dot{\mathbf{y}} + \mathbf{R}^T\mathbf{K}_t^T\mathbf{y} \tag{4.11}$$

$$\mathbf{I}_{mb}\ddot{\Theta}_{mb} + \mathbf{C}_{pg}\dot{\Theta}_{mb} + \mathbf{K}_{pg}\Theta_{mb} = \mathbf{M} + \mathbf{C}_{pg}\dot{\Theta}_d + \mathbf{K}_{pg}\Theta_d \tag{4.12}$$

where:

$$\mathbf{m}=\begin{pmatrix} m_1 & 0 \\ 0 & m_2 \end{pmatrix};\ \mathbf{C}_x=\begin{pmatrix} c_{x1} & 0 \\ 0 & c_{x2} \end{pmatrix};\ \mathbf{K}_x=\begin{pmatrix} k_{x1} & 0 \\ 0 & k_{x2} \end{pmatrix};\ \mathbf{x}=\begin{pmatrix} x_1 \\ x_2 \end{pmatrix};$$

$$\mathbf{y}=\begin{pmatrix} y_1 \\ -y_2 \end{pmatrix};\ \mathbf{C}_y=\begin{pmatrix} c_t+c_{y1} & c_t \\ -c_t & -c_t+c_{y2} \end{pmatrix};\ \mathbf{K}_y=\begin{pmatrix} k_t+k_{y1} & k_t \\ -k_t & -k_t+k_{y2} \end{pmatrix};$$

$$\mathbf{C}_t=\begin{pmatrix} c_t \\ c_t \end{pmatrix};\quad \mathbf{K}_t=\begin{pmatrix} k_t \\ k_t \end{pmatrix};\quad \mathbf{R}=\begin{pmatrix} R_{b1} & R_{b2} \end{pmatrix};\quad \Theta_{12}=\begin{pmatrix} \theta_1 & 0 \\ 0 & -\theta_2 \end{pmatrix};$$

$$\mathbf{I}_{12}=\begin{pmatrix} I_1 & 0 \\ 0 & I_2 \end{pmatrix};\quad \Theta_d=diag(\Theta_{12});\quad \mathbf{C}_z=\begin{pmatrix} R_{b1}^2c_t+c_p & R_{b1}R_{b2}c_t \\ R_{b1}R_{b2}c_t & R_{b2}^2c_t+c_g \end{pmatrix};$$

$$\mathbf{K}_z=\begin{pmatrix} R_{b1}^2k_t+k_p & R_{b1}R_{b2}k_t \\ R_{b1}R_{b2}k_t & R_{b2}^2k_t+k_g \end{pmatrix};\ \mathbf{C}_{pg}=\begin{pmatrix} c_p & 0 \\ 0 & c_g \end{pmatrix};\ \mathbf{K}_{pg}=\begin{pmatrix} k_p & 0 \\ 0 & k_g \end{pmatrix};$$

$$\Theta_{mb}=\begin{pmatrix} \theta_m \\ -\theta_b \end{pmatrix};\qquad \mathbf{I}_{mb}=\begin{pmatrix} I_m & 0 \\ 0 & I_b \end{pmatrix};\qquad \mathbf{M}=\begin{pmatrix} M_1 \\ M_2 \end{pmatrix};$$

Equation (4.9) shows that the vibration in x direction is free response. For free response, when system is stable, the vibration in this direction will disappear due to the inherent damping[36].

Equation (4.10) represents that the system will undergo forced response in y direction. The irritation force is due to the time-varying mesh stiffness and damping, i.e. the periodic time-varying stiffness makes gear system response persist.

4.2.1 The Response of System in x Direction

For Equation (4.9), which is standard equation of motion for free vibration, we can obtain the analytical solutions for different damped cases as follows [36].

a. For underdamped case $(\zeta_i < 1)$

$$x_i(t) = A_i e^{-\zeta_i \omega_i t} \sin(\omega_{d_i} t + \Phi_i) \tag{4.13}$$

where $i = 1, 2$ represent the pinion and the gear, respectively. Symbols in Equation (4.13) are defined as follows.

$$\zeta_i = \frac{c_i}{2\sqrt{k_i m_i}}; \qquad \omega_i = \sqrt{\frac{k_i}{m_i}}; \qquad \omega_{d_i} = \omega_i \sqrt{1 - \zeta_i^2};$$

$$A_i = \sqrt{\frac{(v_{0_i} + \zeta_i \omega_i x_{0_i})^2 + (x_{0_i} \omega_{d_i})^2}{\omega_{d_i}^2}}; \quad \Phi_i = \arctan \frac{x_{0_i} \omega_{d_i}}{v_{0_i} + \zeta_i \omega_i x_{0_i}}$$

where x_{0_i} and v_{0_i} are the initial displacement and velocity of gears, respectively.

Correspondingly, the velocities of gears at time t can be obtained by differentiating the displacement x in Equation (4.13). The result is as follows.

$$\dot{x}_i(t) = A_i e^{-\zeta_i \omega_i t}[-\zeta_i \omega_i \sin(\omega_{d_i} t + \Phi_i) + \omega_{d_i} \cos(\omega_{d_i} t + \Phi_i)] \tag{4.14}$$

Once the derivative of the velocity function in Equation (4.14) is calculated, we obtain the expression of the acceleration shown as follows.

$$\ddot{x}_i(t) = A_i e^{-\zeta_i \omega_i t}[(\zeta_i^2 \omega_i^2 - \omega_{d_i}^2) \sin(\omega_{d_i} t + \Phi_i) - 2\zeta_i \omega_i \omega_{d_i} \cos(\omega_{d_i} t + \Phi_i)] \tag{4.15}$$

From Equation (4.15), it is seen that the acceleration of gear vibration in

x direction is an exponential-attenuation periodic function of time.

b. For overdamped case $(\zeta_i > 1)$

In this case, the displacement, velocity and acceleration of gear vibration can be expressed as Equations (4.16)-(4.18), respectively.

$$x_i(t) = e^{-\zeta_i \omega_i t}(a_{1_i} e^{-\sqrt{\zeta_i^2-1}\,\omega_i t} + a_{2_i} e^{\sqrt{\zeta_i^2-1}\,\omega_i t}) \tag{4.16}$$

$$\dot{x}_i(t) = \omega_i e^{-\zeta_i \omega_i t}\Big[-\Big(\zeta_i+\sqrt{\zeta_i^2-1}\,\Big)a_{1_i} e^{-\sqrt{\zeta_i^2-1}\,\omega_i t} - \Big(\zeta_i-\sqrt{\zeta_i^2-1}\,\Big)a_{2_i} e^{\sqrt{\zeta_i^2-1}\,\omega_i t}\Big] \tag{4.17}$$

$$\ddot{x}_i(t) = \omega_i^2 e^{-\zeta_i \omega_i t}\Big[\Big(\zeta_i+\sqrt{\zeta_i^2-1}\,\Big)^2 a_{1_i} e^{-\sqrt{\zeta_i^2-1}\,\omega_i t} + \Big(\zeta_i-\sqrt{\zeta_i^2-1}\,\Big)^2 a_{2_i} e^{\sqrt{\zeta_i^2-1}\,\omega_i t}\Big] \tag{4.18}$$

where:

$$a_{1_i} = \frac{-v_{0_i} - \Big(\zeta_i - \sqrt{\zeta_i^2-1}\,\Big)\omega_i x_{0_i}}{2\omega_i\sqrt{\zeta_i^2-1}}; \quad a_{2_i} = \frac{v_{0_i} + \Big(\zeta_i + \sqrt{\zeta_i^2-1}\,\Big)\omega_i x_{0_i}}{2\omega_i\sqrt{\zeta_i^2-1}};$$

From Equation (4.18), it is observed that the acceleration of gear vibration in x direction is an exponential-attenuation function of time.

c. For critically damped case $(\zeta_i = 1)$

In this case, we can calculate the displacement, velocity and acceleration of gear vibration according to Equations (4.19)-(4.21), respectively.

$$x_i(t) = e^{-\omega_i t}(b_{1_i} + b_{2_i} t) \tag{4.19}$$

$$\dot{x}_i(t) = -\omega_i e^{-\omega_i t}\Big[\Big(b_{1_i} - \frac{b_{2_i}}{\omega_i}\Big) + b_{2_i} t\Big] \tag{4.20}$$

$$\ddot{x}_i(t) = \omega_i^2 e^{-\omega_i t}\left[\left(b_{1_i} - \frac{2b_{2_i}}{\omega_i}\right) + b_{2_i} t\right] \tag{4.21}$$

where: $b_{1_i} = x_{0_i}$; $\quad b_{2_i} = v_{0_i} + \omega_i x_{0_i}$

From Equation (4.21), it is once again observed that the acceleration of gear vibration in x direction is an exponential-attenuation function of time.

Therefore, for all above three cases, the results show that the vibration acceleration response in x direction will fade out with time, i.e., when the system is stable, the vibration in x direction is transient and will disappear.

4.2.2 The Response of System in y Direction

Since the response in x direction is transient, we will focus on the acceleration response in y direction, which represents the effect of time-varying mesh stiffness.

For Equations (4.3)-(4.8), the analytical solutions can not be obtained since both torsional and lateral vibrations are coupled in this equation group. Therefore, numerical solutions have to be pursued for studying the system response due to time-varying mesh stiffness. In the following sections, we will discuss the corresponding system responses in y direction for different situations of gears, i.e. perfect gears, the pinion with a chipped tooth, the pinion with a cracked tooth and the pinion with a broken tooth.

4.3 Dynamic Simulation for Perfect Gears

In order to investigate the vibration responses for gear system including the pinion with local tooth faults, it is necessary to know the response of perfect gear system. For the perfect gear system, we assume that all components including gears, motor, shafts and bearings have no manufacturing and as-

semblage errors. In addition, it is assumed that the lubrication condition is perfect.

For the purpose of simulation simplification, we assume that the radial stiffnesses k_{x1}, k_{y1}, k_{x2} and k_{y2} of four bearings are equal to a constant k_r. In addition, the damping coefficients c_{x1}, c_{y1}, c_{x2} and c_{y2} of bearings will be made equal to a constant c_r. Finally, the torsional stiffnesses and the damping coefficients of the input and output couplings are equal to k_c and c_c, respectively, i.e. $k_p = k_g = k_c$, $c_p = c_g = c_c$.

In this study, the main parameters of the gear system applied in this model are listed in Table 4.1. These values are chosen partly referring to the parameters of *Gearbox Dynamics Simulator*.

In this study, we assume that the system has a constant damping ratio 0.07 ($\zeta = 0.07$, refer to [7]), and the mesh damping coefficient is proportional to the mesh stiffness [4], i.e.

$$c_t = \mu k_t \tag{4.22}$$

where μ is the scale constant with units of $second\,(s)$.

To determine the constant μ, we consider the mean values k_m and c_m of the mesh stiffness and the mesh damping coefficient within one mesh period. For the applied gear pair in this study, $k_m = 8.854 \times 10^8\,(N/m)$. The damping ratio can be calculated by [36]:

$$\zeta = \frac{c_m}{2\sqrt{k_m m}} \tag{4.23}$$

where m is the effective mass of pinion and gear. It can be expressed as [4]:

$$m = \frac{m_1 m_2}{m_1 + m_2} \tag{4.24}$$

Table 4.1: Main parameters of the gear system

Gear type	standard involute spur teeth
Material	steel
Young's modulus	$E = 2.068 \times 10^{11} Pa$ [35]
Poisson's ratio	$\nu = 0.3$ [35]
Number of teeth	$N_1 = 19$ *and* $N_2 = 48$
Pressure angle	$\alpha_0 = 20^\circ$
Diametral pitch	$P = 8\ inch^{-1}$
Base radius of the pinion	$R_{b1} = 0.02834\ m$
Base radius of the gear	$R_{b2} = 0.07160\ m$
Width of teeth	$L = 0.016\ m$
Mass of the pinion	$m_1 = 0.96\ kg$
Mass of the gear	$m_2 = 2.88\ kg$
Contact ratio	$C_r = 1.6456$
Mass moment of inertia of the motor	$I_m = 0.0021\ kgm^2$ [37]
Mass moment of inertia of the load	$I_b = 0.0105\ kgm^2$ [37]
Mass moment of inertia of the pinion	$I_1 = m_1 R_{p1}^2/2 = 4.3659 \times 10^{-4}\ kgm^2$
Mass moment of inertia of the gear	$I_2 = m_2 R_{p2}^2/2 = 8.3602 \times 10^{-3}\ kgm^2$
Input shaft frequency	$f_1 = 30\ Hz$
Mesh frequency	$f_m = 570\ Hz$
Input motor torque	$M_1 = 11.9\ Nm$ [37]
Output load torque	$M_2 = 48.8\ Nm$ [37]
Torsional stiffness of the coupling	$k_c = 4.4 \times 10^4\ Nm/rad$ [38]
Damping coefficient of the coupling	$c_c = 5.0 \times 10^5\ Nms/rad$ [38]
Radial stiffness of the bearing	$k_r = 6.56 \times 10^7\ N/m$ [38]
Damping coefficient of the bearing	$c_r = 1.8 \times 10^5\ Ns/m$ [38]

Substitute m into Equation (4.23), we can obtain the expression of c_m:

$$c_m = 2\zeta\sqrt{k_m \frac{m_1 m_2}{m_1 + m_2}} \tag{4.25}$$

Substitute the values of ζ, k_m, m_1 and m_2 (listed in Table 4.1) into Equation (4.25), we get $c_m = 3.533 \times 10^3\,(Ns/m)$. Thus, we select $\mu = c_m/k_m = 3.99 \times 10^{-6}(s)$.

So far, we have determined all parameters used in equations of motion. For Equations (4.3-4.8), we can not get the analytical solutions. Instead, we have to pursue the numerical solutions. During pursuing numerical solutions, the trade-offs between step-size, round-off errors and complexity of the algorithms have to be considered. Generally, the smaller the step-size, the higher the calculation accuracy, but the bigger the accumulated round-off errors. To circumvent this problem, one makes use of higher order routines, which yield improved accuracy with larger step sizes.

MATLAB's ODE15s function will be used to obtain numerical solutions to the equations of motion. (In general, ODE45, which is based on 4^{th}-5^{th} Runge-Kutta method, is considered as the best function to apply as a "first try" for most problems. When ODE45 fails, or is very inefficient, or the problem is suspected to be stiff, ODE15s is a better choice. For the above equation group, as a 'first try', ODE45 failed. On the basis of the above explanation, ODE15s is selected.)

Figure 4.2 shows the vibration acceleration response of the gear system within two shaft rotation periods (shaft period $T_1 = 1/f_1 = 0.0333\,(s)$). One shaft period T_1 consists of 19 mesh periods T_m. The acceleration response of the pinion (shown in Figure 4.2(a)) is much stronger than that of the gear

(shown in Figure 4.2(b)) in that the pinion is much lighter than the mating gear. The amplitudes are not symmetrical about zero because the peaks correspond to the shock from the double-tooth-pair duration to the single-tooth-pair duration. However, the valleys correspond to the shock from the single-tooth-pair duration to the double-tooth-pair duration.

To observe the details, we provide the response plots (Figure 4.3) within two mesh periods. Without loss of generality, we select the first two mesh periods during the second shaft period. In Figure 4.3, A_1 and A_2, which correspond to time $t = T_1$, are the beginning points of the second shaft period for the pinion and the gear, respectively. The responses present periodic attenuated oscillations. The oscillation period T_{nd} is $0.264ms$. At the points B_1 and B_2, the oscillations are excited anew. B_1 and B_2 correspond to the transition point from double-tooth-pair mesh to single-tooth-pair mesh. The duration of the double-tooth-pair contact is T_d. From point B_1/B_2 to point C_1/C_2, the gear system undergoes the single-tooth-pair duration T_s. The responses also present periodic attenuated oscillations. The corresponding oscillation period T_{ns} is $0.328ms$. At points C_1 and C_2, which correspond to the transition point from single-tooth-pair mesh to double-tooth-pair mesh, the new mesh period begins. Thus, each mesh period consists of two components T_d and T_s.

The corresponding amplitude spectra of the acceleration responses are shown in Figure 4.4. In this thesis, we use the unit dB to express the amplitudes of the vibration acceleration in the frequency domain. The reference vibration acceleration is $10^{-5}\ m/s^2$ [41]. As expected, it is observed that spectra comprise harmonics of the gear meshing frequency, among which the sixth harmonic meshing frequency ($3420Hz$) dominates the frequency response. Consider oscillation periods T_{nd} and T_{ns} in Figure 4.3. The corre-

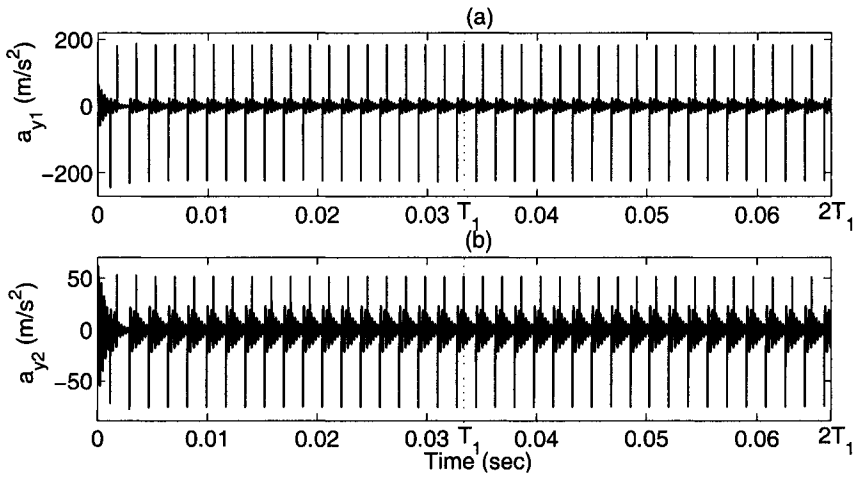

Figure 4.2: The vibration acceleration response a_y in y direction for perfect gears within two shaft periods: (a) The pinion; (b) The gear: T_1 - the shaft period; a_{y1} - the acceleration for the center of the pinion; a_{y2} - the acceleration for the center of the gear.

sponding oscillation frequencies are $3788Hz$ and $3049Hz$, respectively. The mean of these two oscillation frequencies is 3418Hz, which is very close to the sixth harmonic meshing frequency.

In comparison, based on the mesh stiffness shown in Figure 2.9 on page 47, the spectra of the acceleration responses without the shear stiffness considered are shown in Figure 4.5. It is found that the eighth harmonic meshing frequency dominates the frequency response instead of the sixth harmonic in the case with the shear stiffness considered.

Thus, for a pair of gears with perfect teeth, the vibration of gears is periodic with mesh period T_m. Within each T_m, the vibration includes a peak point and a valley point. The time span from the peak to the valley is T_d. The span from the valley to the peak is T_s. In the frequency domain, the waveforms are dominated by the attenuated oscillation frequency of the gear system. No shaft frequency can be observed.

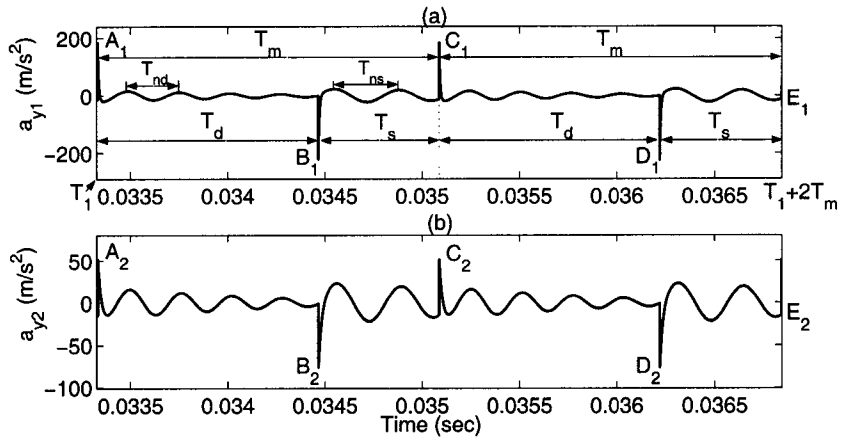

Figure 4.3: The vibration acceleration response a_y in y direction for perfect gears within two mesh periods: (a) The pinion; (b) The gear: T_1 - the shaft period; T_m - the mesh period; T_d - the double-tooth-pair duration; T_s - the single-tooth-pair duration; a_{y1} - the acceleration for the center of the pinion; a_{y2} - the acceleration for the center of the gear.

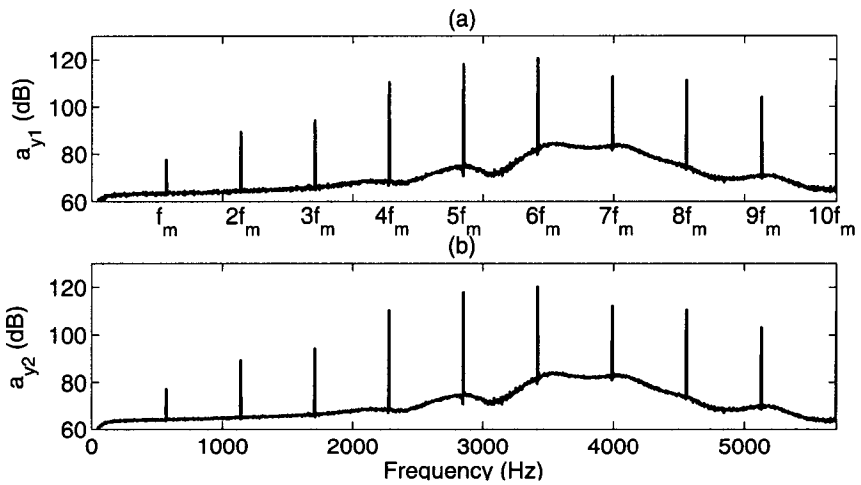

Figure 4.4: Spectra of the vibration acceleration response a_y in y direction for perfect gears: (a) The pinion; (b) The gear: a_{y1} - the acceleration for the center of the pinion; a_{y2} - the acceleration for the center of the gear.

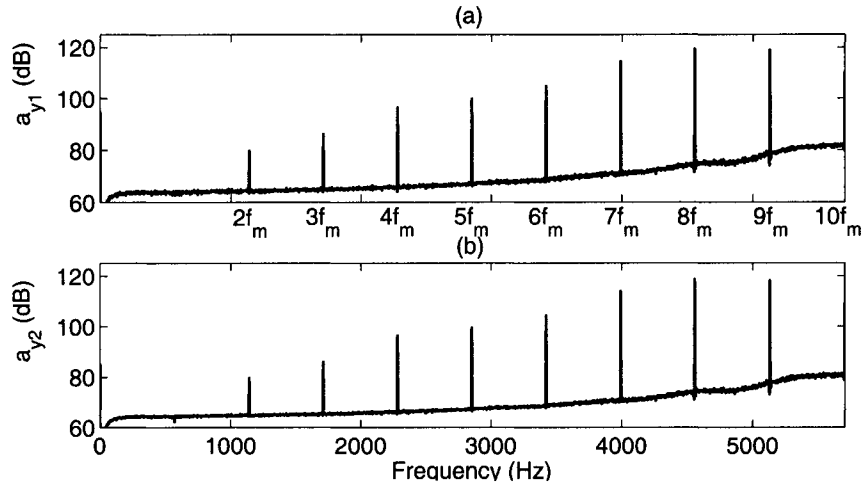

Figure 4.5: Spectra of the vibration acceleration response a_y in y direction for perfect gears with the shear energy ignored: (a) The pinion; (b) The gear: a_{y1} - the acceleration for the center of the pinion; a_{y2} - the acceleration for the center of the gear.

4.4 Dynamic Simulation for Pinion with a Chipped Tooth

The vibration acceleration response of gear system with a chipped tooth on the pinion is shown in Figure 4.6 and Figure 4.7 for two shaft periods and two mesh periods, respectively. The two relatively small peaks in Figure 4.6 reflect the presence of the chipped fault. The span between these two peaks is the shaft period T_1. In Figure 4.7, from points A_1 and A_2, the response curves of gear system in chipped case and perfect case begin separating. Instead of the attenuated oscillation of perfect gear system, the system undergoes a new excitation at time $t = 0.0354s$, which corresponds to the angular displacement $\theta_1 = 22.4°$, which is the initial point of the chipped part on the pinion. Due to the decrease of the mesh stiffness drop at transition point from double-tooth-pair mesh to single-tooth-pair mesh (E instead of F in Figure 3.2), the corresponding excitation response decreases at the transition point (as shown

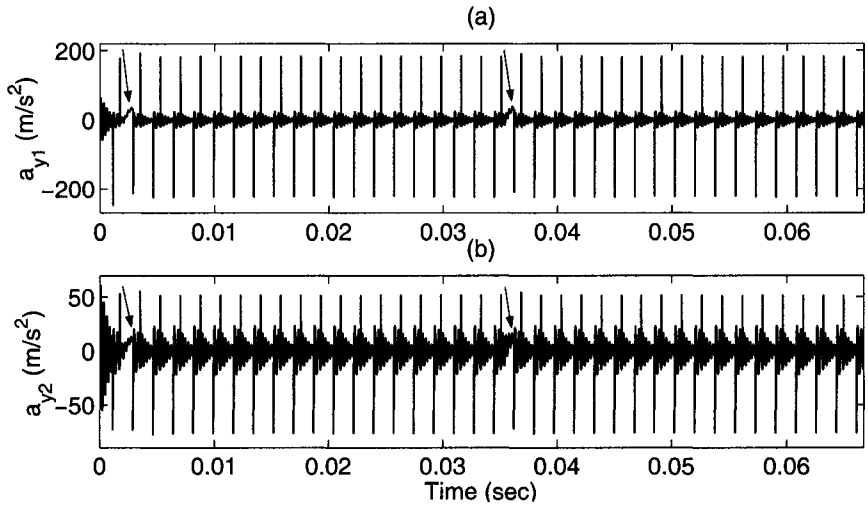

Figure 4.6: The vibration acceleration response a_y in y direction for the pinion with a chipped tooth within two shaft periods: (a) The pinion; (b) The gear: T_1 - the shaft period; a_{y1} - the acceleration for the center of the pinion; a_{y2} - the acceleration for the center of the gear.

in Figure 4.7).

Figure 4.8 shows the corresponding amplitude spectra. We see that the frequency responses are still dominated by the sixth harmonic meshing frequency, which is very close to the oscillation frequency of the system. It is also observed that the fundamental shaft frequency and its harmonics appear.

In the chipped case, the vibration of gears still includes mesh period T_m. Compared with the vibration in the perfect case, however, relatively lower peaks appear in every shaft period T_1. And the magnitude of the following adjacent valley decreases. Spectra of the responses consist of harmonics of the meshing frequency and the shaft frequency.

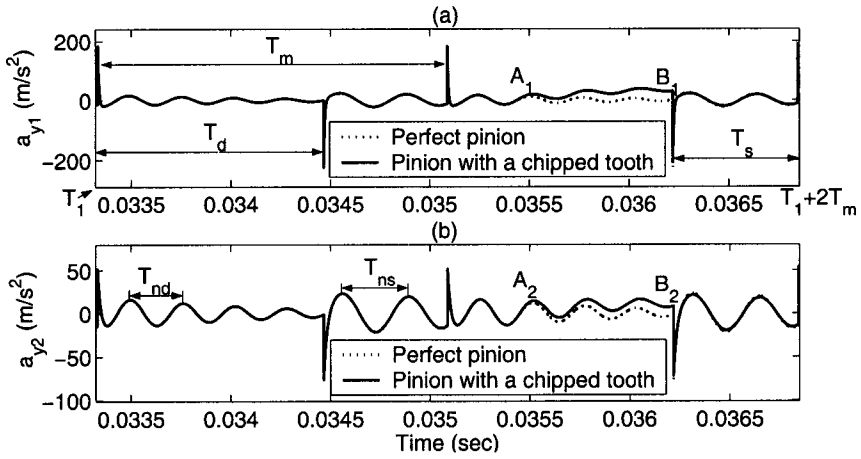

Figure 4.7: The vibration acceleration response a_y in y direction for the pinion with a chipped tooth within two mesh periods: (a) The pinion; (b) The gear: T_1 - the shaft period; T_m - the mesh period; T_d - the double-tooth-pair duration; T_s - the single-tooth-pair duration; a_{y1} - the acceleration for the center of the pinion; a_{y2} - the acceleration for the center of the gear.

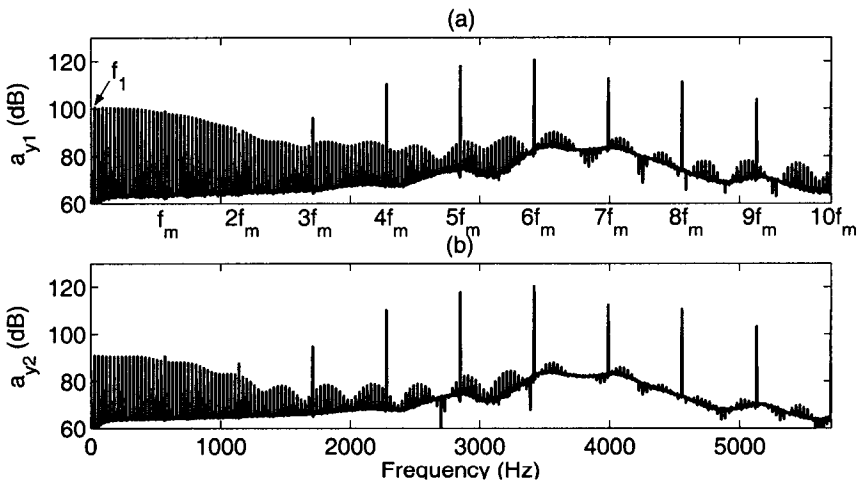

Figure 4.8: Spectra of the vibration acceleration response a_y in y direction for the pinion with a chipped tooth: (a) The pinion; (b) The gear: a_{y1} - the acceleration for the center of the pinion; a_{y2} - the acceleration for the center of the gear.

4.5 Dynamic Simulation for Pinion with a Cracked Tooth

The acceleration responses of the gear system with a cracked tooth on the pinion are shown in Figure 4.9 and Figure 4.10. In Figure 4.9, two peaks appear, which represent the mating of the cracked tooth. The span between these two peaks is the shaft period T_1. Figure 4.10 clearly reflects the influence of the crack. Within first double-tooth-pair duration T_d, the response has no obvious change. From time $t = T_1 + T_d$ to $t = T_1 + T_m + T_d$, there is a marked increase in the vibration acceleration. After $t = T_1 + T_m + T_d$, the oscillation attenuates, because the drop of mesh stiffness at the transition point from double-tooth-pair mesh to single-tooth-pair mesh decreases due to the crack, i.e. the excitation decreases at this point.

Figure 4.11 shows the corresponding amplitude spectra. It is found that the frequency response in the pinion is dominated by harmonics of the shaft frequency. The second peak appears at the sixth harmonic meshing frequency.

Compared with the case for the existence of a tooth chip, the vibration response due to a tooth crack has a wider influence range and higher peak values reflecting the mating of the cracked tooth.

The vibration of gears still includes mesh period T_m. Compared with the vibration in the perfect case, however, in this cracked case, relatively higher peaks appear in every shaft period T_1. As well, the magnitude of the preceding adjacent peak, which represents the transition point from single-tooth-pair mesh to double-tooth-pair mesh, will be much higher than that in perfect case. However, the magnitude of the following adjacent valley, which represents the transition point from double-tooth-pair mesh to single-tooth-pair mesh, will be much smaller than that in perfect case.

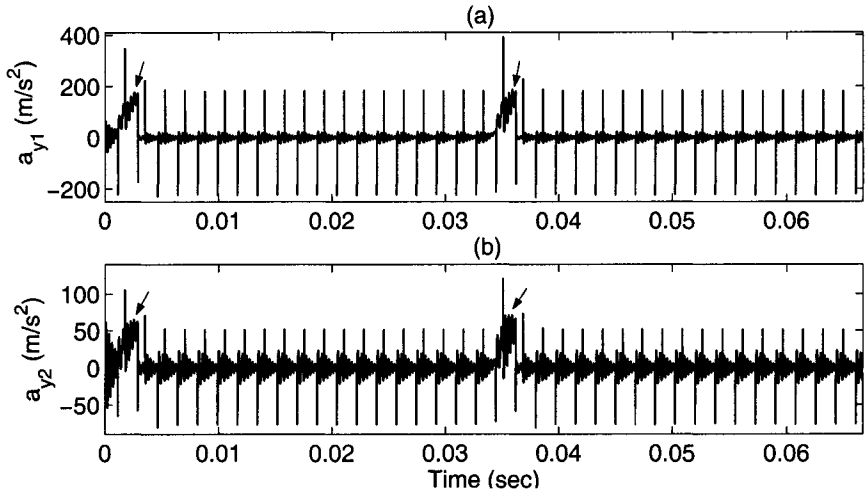

Figure 4.9: The vibration acceleration response a_y in y direction for the pinion with a cracked tooth within two shaft periods: (a) The pinion; (b) The gear: T_1 - the shaft period; a_{y1} - the acceleration for the center of the pinion; a_{y2} - the acceleration for the center of the gear.

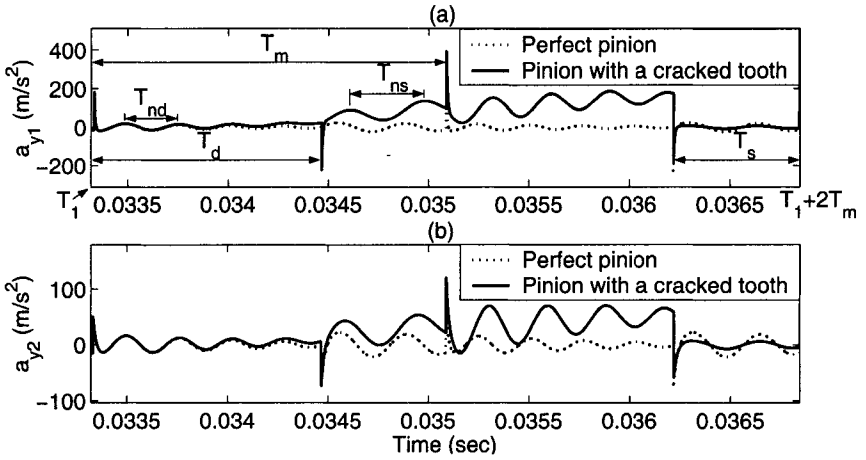

Figure 4.10: The vibration acceleration response a_y in y direction for the pinion with a cracked tooth within two mesh periods: (a) The pinion; (b) The gear: T_1 - the shaft period; T_m - the mesh period; T_d - the double-tooth-pair duration; T_s - the single-tooth-pair duration; a_{y1} - the acceleration for the center of the pinion; a_{y2} - the acceleration for the center of the gear.

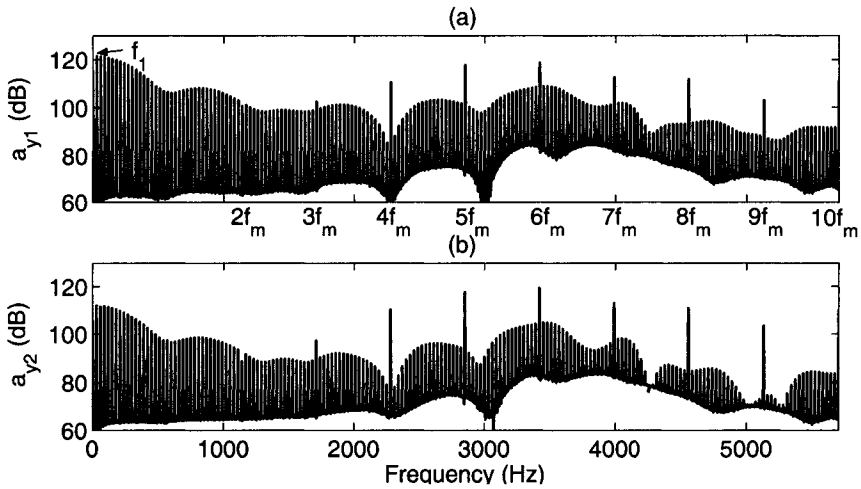

Figure 4.11: Spectra of the vibration acceleration response a_y in y direction for the pinion with a cracked tooth: (a) The pinion; (b) The gear: a_{y1} - the acceleration for the center of the pinion; a_{y2} - the acceleration for the center of the gear.

4.6 Dynamic Simulation for Pinion with a Broken Tooth

When there is a broken tooth in the pinion, the vibration response is shown in Figure 4.12 and Figure 4.13. In Figure 4.12, there are two peaks with quite high amplitudes, which represent the shock caused from the reestablishment of the the mating of teeth after the losing of the mating. The span between peaks is the shaft period T_1. Figure 4.13 clearly shows the corresponding point A, which corresponds to time $t = T_1 + T_m$. Beginning with point A, the system undergoes periodic attenuated oscillations. The oscillation period T_{ndb} is $0.395ms$. The corresponding oscillation frequency is $2530Hz$.

The corresponding amplitude spectra are shown in Figure 4.14. We see that spectra mainly consist of harmonics of the shaft frequency. No meshing frequency and its harmonics can be observed. The peak P corresponds to the frequency $2370Hz$, which is close to the oscillation frequency $2530Hz$. Thus in

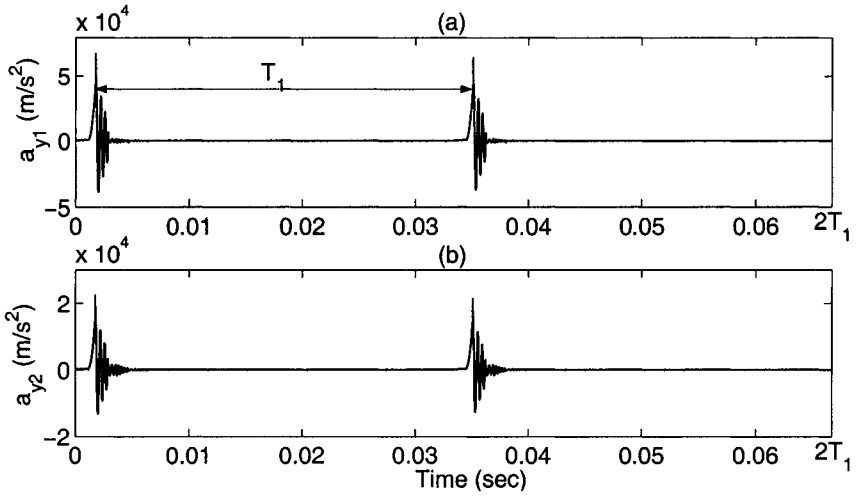

Figure 4.12: The vibration acceleration response a_y in y direction for the pinion with a broken tooth within two shaft periods: (a) The pinion; (b) The gear: T_1 - the shaft period; a_{y1} - the acceleration for the center of the pinion; a_{y2} - the acceleration for the center of the gear.

this broken case, the vibration response of gears is dominated by the oscillation caused by the tooth breakage.

4.7 Summary

In this chapter, we investigated the vibration acceleration responses of the one-stage gear system with 19/48 gear pair. For the vibration in the direction parallel to teeth in mesh, we obtained the analytical solutions. The results show that the vibration in this direction is transient when the system is stable. For the response in the direction vertical to teeth in mesh, the numerical solutions are pursued for perfect gears, the pinion with a tooth chip, a tooth crack and a tooth breakage, respectively. For each case, the mesh stiffness variation is studied. The results validate the expressions derived by us in Chapter 3, which are applied for the investigation of the vibration acceleration

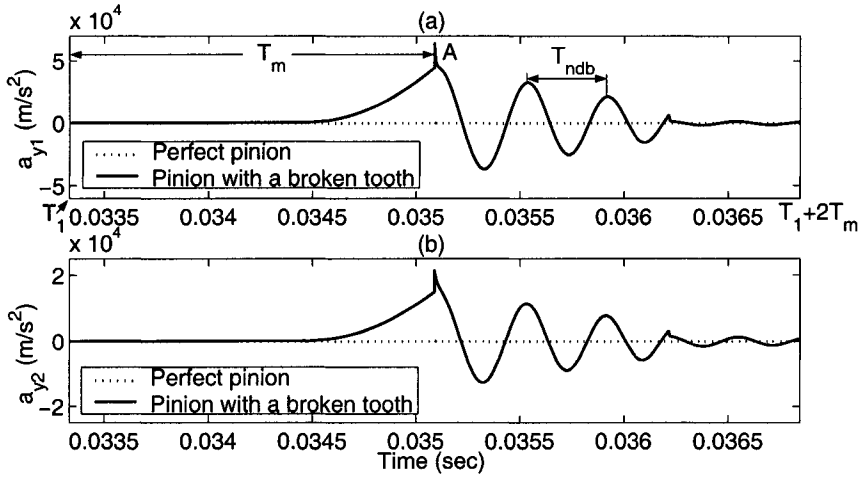

Figure 4.13: The vibration acceleration response a_y in y direction for the pinion with a broken tooth within two mesh periods: (a) The pinion; (b) The gear: T_1 - the shaft period; T_m - the mesh period; a_{y1} - the acceleration for the center of the pinion; a_{y2} - the acceleration for the center of the gear.

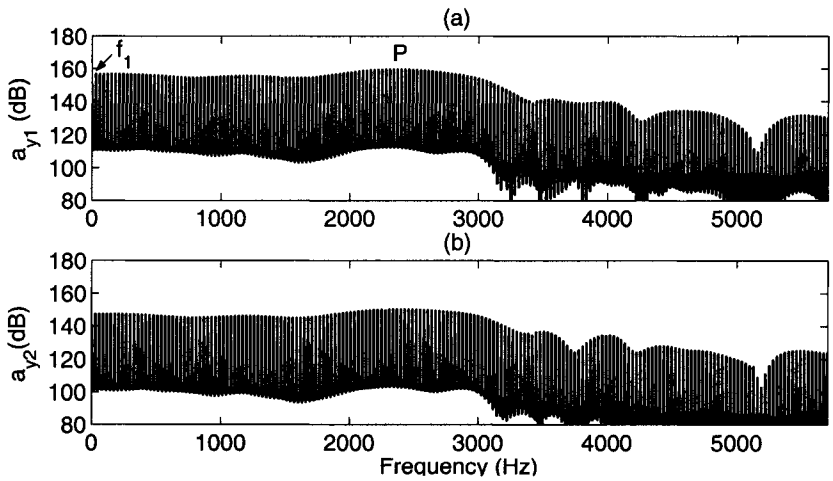

Figure 4.14: Spectra of the vibration acceleration response a_y in y direction for the pinion with a broken tooth: (a) The pinion; (b) The gear: a_{y1} - the acceleration for the center of the pinion; a_{y2} - the acceleration for the center of the gear.

responses. The acceleration responses in different local tooth faults are changed in comparison to that in perfect case. The results are consistent with the corresponding change properties of the mesh stiffness, i.e. the mesh stiffness variation causes the change of the vibration acceleration response.

In the perfect case, the vibration of gears is periodic with the mesh period. Within each mesh period, the vibration includes a peak point and a valley point. The time span from the peak to the valley is the duration of the double-tooth-pair. The span from the valley to the peak is the duration of the single-tooth-pair. No shaft period is observed. The frequency response is dominated by the oscillation frequency of the system. In comparison, relatively lower peaks appear in every shaft period for the chipped fault. The magnitude of the following adjacent valley decreases. The spectra present the harmonics of the shaft frequency and the prominent peak at the sixth harmonic meshing frequency, which is close to the oscillation frequency of the system. Compared with the case for the existence of a tooth chip, the vibration response due to a tooth crack has a wider influence range and higher peak values reflecting the mating of the cracked tooth. In comparison with the vibration in the perfect case, however, relatively higher peaks appear in every shaft period. And the magnitude of the preceding adjacent peak is much higher as well. However, the magnitude of the following adjacent valley is much smaller than that in perfect case. The frequency response in the pinion is dominated by the shaft frequency and its harmonics. There exists another peak near the oscillation frequency of the system. For the broken case, the vibration of gears is dominated by very high peaks appearing in every shaft period. And no obvious mesh period was observed. The frequency response is dominated by the oscillation caused by the tooth breakage.

Chapter 5

Conclusions and Further Research

In this study, we investigated the vibration responses of the gear system with local tooth faults by a one-stage involute spur gear dynamic model. We introduce a method of local tooth fault simulation, i.e., the parameter mesh stiffness of mating teeth, by which three kinds of typical local tooth faults are simulated based on the geometry properties of involute spur gears.

The direct calculation formulae of mesh stiffness are provided based on the potential energy method proposed by Yang and Lin [21]. In this study, the shear energy, which was not considered in the study of Yang and Lin, is included. It was found that the shear energy affected the total energy by factor 2. Compared with axial compressive and bending energies, the shear energy had a larger influence on the total energy.

In this study, expressions for calculating the lasting angles of the double- and single-tooth-pair mesh durations within one mesh period are derived and validated by a parametric comparison method. To complete the model, the expressions of the effective mesh stiffness of mating gears with three kinds of localized tooth faults are also derived. These faults include: a chipped tooth, a cracked tooth, and a broken tooth.

It was found that a thin tooth chip of the pinion will mainly influence the Hertzian contact stiffness of the mating teeth, which determines the variation of the total mesh stiffness in this fault. Bending, shear and axial compressive stiffnesses are not significantly affected.

In examining the cracked fault, bending and shear stiffnesses are greatly influenced due to the existence of a crack. Hertzian contact stiffness and axial compressive stiffness, however, are considered unaltered in comparison with those for the perfect case. The influence of the crack on the total mesh stiffness is larger than that in the chipped case.

As expected, a tooth breakage totally alters the mesh stiffness. It causes great drop and rise at the transition points of single/double-tooth-pair mesh.

With the help of these parameter expressions, the corresponding vibration acceleration responses of the 19/48 gear system were simulated under the perfect and faulty cases.

In the perfect case, the vibration of gears is periodic with the mesh period. Within each mesh period, the vibration includes a peak point and a valley point. The time span from the peak to the valley is the duration of the double-tooth-pair. The span from the valley to the peak is the duration of the single-tooth-pair. No shaft period was observed. The spectra display the harmonics of the meshing frequency and the prominent peak at the sixth harmonic meshing frequency, which is very close to the oscillation frequency of the system. In addition, the shear stiffness had an influence upon the dominant frequency of the spectra. Instead of the sixth harmonic, the eighth harmonic meshing frequency dominated the spectra without the shear stiffness considered.

In comparison, for the chipped fault, relatively lower peaks appear in every

shaft period. The magnitude of the following adjacent valley decreases. The mesh period was still observed in the vibration response of gears. The frequency responses were dominated by the oscillation frequency of the system. It was also observed that the fundamental shaft frequency and its harmonics appear.

Unlike that of a chipped tooth, the vibration response of a cracked tooth has a wider influence range and higher peak values reflecting the mating of the cracked tooth. In comparison with the vibration in the perfect case, however, relatively higher peaks appear in every shaft period. And the magnitudes of the preceding adjacent peaks are much higher as well. However, the magnitudes of the following adjacent valleys are much smaller. It was found that the frequency response in the pinion was dominated by harmonics of the shaft frequency. There existed another peak at the sixth harmonic meshing frequency.

For the broken case, the vibration of gears is dominated by very high peaks appearing in every shaft period. And there was no obvious mesh period observed. The frequency response was dominated by the oscillation caused by the tooth breakage.

The results show that the properties of the responses are consistent with the variations of mesh stiffness, which indicates the effectivity of the mesh stiffness as the introduction parameter of local tooth faults.

The results in this thesis can be used to understand the signatures of gear faults. They are also helpful to study on advanced signal processing techniques for fault diagnosis.

Based on the study in this thesis, possible further researches can be listed as follows.

- Experimental study on dynamic response of one-stage gear system (Some

faults can be set according to the model used in this thesis.);

- The time-varying mesh damping coefficient investigation (In this thesis, the mesh damping coefficient was considered constant. Based on the results of this thesis, the time-varying damping coefficient can be studied to get closer to reality.);
- Similar study on dynamic response of two-stage gear system. Further, study on signal processing techniques for fault diagnosis;
- Dynamic response of one-stage gear system considering errors (In this thesis, the dynamic responses under ideal cases were investigated. Based on this, errors such as manufacture error and friction can be introduced.);
- Study on dynamic response of gearbox system considering vibration propagation in a nonrigid casing (In this thesis, the gearbox casing was assumed rigid).

BIBLIOGRAPHY

[1] D. P. Townsend, *Gear Handbook*, McGRAW-HILL, INC., 1992.

[2] H. Nevzat zgven and D. R. Houser, "Mathematical Models Used in Gear Dynamics-A Review," *Journal of Sound and Vibration*, **121**(3), pp. 383-411, 1988.

[3] F. L. Litvin, *Gear Geometry and Applied Theory*, Prentice-Hall, Inc., 1994.

[4] M. Amabili and A. Rivola, "Dynamic Analysis of Spur Gear Pairs: Steady-state Response and Stability of the SDOF Model with Time-varying Meshing Damping," *Mechanical Systems and Signal Processing*, **11**(3), pp. 375-390, 1997.

[5] A. Fisher, "Factors in Calculating the Load-carrying Capacity of Helical Gears," *Machinery*, 98, pp. 545-552, 1961.

[6] E. J. Wellauer, "An Analysis of Factors Used for Strength Rating Helical Gears," *American Society of Mechanical Engineers Paper 59-A-121*, 1959.

[7] S. L. Harris, "Dynamic Loads on the Teeth of Spur Gears," *Proceedings of the Institution of Mechanical Engineers*, 172, pp. 87-112, 1958.

[8] R. W. Gregory, S. L. Harris and R. G. Munro, "Dynamic behavior of Spur Gears," *Proceedings of the Institution of Mechanical Engineers*, 178, pp. 207-226, 1964.

[9] R. W. Gregory, S. L. Harris and R. G. Munro, "Torsional Motion of A Pair of Spur Gears," *Proceedings of the Institution of Mechanical Engineers*, 178, pp. 166-173, 1964.

[10] K. Ishida and T. Matsuda, "Study on Pitch Circle Impulse Noise of Gear," *American Society of Mechanical Engineers Paper 80-C2/DET-69*, 1980.

[11] K. Ishida and T. Matsuda, "Effect of Tooth Surface Roughness on Gear Noise and Gear Noise Transmitting Path," *American Society of Mechanical Engineers Paper 80-C2/DET-70*, 1980.

[12] D. Lewicki, "Predicted Effect of Dynamic Load on Pitting Fatigue Life for Low-contact Ratio Spur Gears," *NASA Technical Paper 2610*, 1986.

[13] H. Fukuma, T. Furukawa and T. Aida, "Fundamental Research on Gear Noise and Vibration (6th Report, Generation Mechanism of Radial and Axial Vibration of Spur Gears)," *Bulletin of the Japanese Society of Mechanical Engineers*, 16, pp. 1094-1107, 1973.

[14] G.N. Lance, *Numerical methods for high-speed computers*, Iliffe & Sons, London, 1960.

[15] G. V. Tordion and R. Gauvin, "Dynamic Stability of a Two-stage gear Train Under the Influence of Variable Meshing Stiffnesses," *Journal of Engineering for Industry, Transactions of the American Society of Mechanical Engineers*, 99, pp. 785-791, 1977.

[16] T. Sakai, Y. Doi, K. Yamamoto, T. Ogasawara and M. Narita, "Theoretical and Experimental Analysis of Rattling Noise of Automotive Gearbox," *Society of Automotive Engineers Paper 810773*, 1981.

[17] A. S. Kumar, T. S. Sankar and M .O. M Osman, "On Dynamic Tooth Load and Stability of A Spur-gear System Using the State-space Approach," *Journal of Mechanisms, Transmissions, and Automation in Design, Transactions of the American Society of Mechanical Engineers* 107, pp. 54-60, 1985.

[18] H. Lida, A. Tamura and Y. Yamada, "Vibrational Characteristics of Friction between Gear Teeth," *Bulletin of the Japanese Society of Mechanical Engineers*, 28, pp. 1512-1519, 1985.

[19] W. Bartelmus, "Mathematical Modeling and Computer Simulations as An Aid to Gearbox Diagnostics" *Mechanical Systems and Signal Processing*, **15**(5), pp. 855-871, 2001.

[20] I. Howard, S. Jia and J. Wang, "The Dynamic Modeling of A Spur Gear in Mesh Including Friction and A Crack," *Mechanical Systems and Signal Processing*, **15**(5), pp. 831-853, 2001.

[21] D.C.H. Yang and J.Y. Lin, "Hertzian Damping, Tooth Friction and Bending Elasticity in Gear Impact Dynamics" *Journal of Mechanisms, Transmissions, and Automation in Design*, 109, pp. 189-196, 1987.

[22] A. Kahraman and R. Singh, "Interactions Between Time-varying Mesh Stiffness and Clearance Non-linearities in a Geared System," *Journal of Sound and Vibration*, 146, pp. 135-156, 1991.

[23] S. Theodossiades and S. Natsiavas, "Nonlinear Dynamics of Gear-pair Systems with Periodic Stiffness and Backlash," *Journal of Sound and Vibration*, **229**(2), pp. 287-310, 2000.

[24] Y. Cai and T. Hayashi, "The Linear Approximated Equation of Vibration of a Pair of Spur Gears (Theory and Experiment)," *Journal of Mechanical Design*, 116, pp. 558-564, 1994.

[25] R. G. Parker, S. M. Vijayakar and T. Imajo, "Nonlinear Dynamic Response of a Spur Gear Pair: Modelling and Experimental Comparisons," *Journal of Sound and Vibration*, **237**(3), pp. 435-455, 2000.

[26] R. G. Parker, V. Agashe and S. M. Vijayakar, "Dynamic Response of a Planetary Gear System using a Finite Element/Contact Mechanics Model," *Journal of Mechanical Design*, 122, pp. 304-310, 2000.

[27] J. H. Kuang and A. D. Lin, "The Effect of Tooth Wear on the Vibration Spectrum of a Spur Gear Pair," *Journal of Vibration and Acoustics*, 123, pp. 311-317, 2001.

[28] J. H. Kuang and A. D. Lin, "Theoretical Aspects of Torque Responses in Spur Gearing Due to Mesh Stiffness Variation," *Mechanical Systems and Signal Processing*, **17**(2), pp. 255-271, 2003.

[29] M. E. Badaoui, V. Cahouet, F. Guillet, J. Daniere and P. Velex, "Modeling and Detection of Localized Tooth Defects in Geared Systems," *Journal of Mechanical Design*, 123, pp. 422-430, 2001.

[30] J. Lin and R. G. Parker, "Mesh Stiffness Variation Instabilities in Two-Stage Gear Systems," *Journal of Vibration and Acoustics*, 124, pp. 68-76, 2002.

[31] A. S. Lee, J. W. Ha and D. Choi, "Coupled Lateral and Torsional Vibration Characteristics of a Speed Increasing Geared Rotor-bearing System," *Journal of Sound and Vibration*, **263**(4), pp. 725-742, 2003.

[32] J. Wojnarowski and V. Onishcheko, "Tooth Wear Effects on Spur Gear Dynamics," *Mechanism and Machine Theory*, 38, pp. 161-178, 2003.

[33] D.C.H. Yang and Z.S. Sun, "A Rotary Model For Spur Gear Dynamics," *ASME Journal of Mechanisms, Transmissions, and Automation in Design*, 85-DET-2, 1985.

[34] J. D. Smith, *Gears and Their Vibration*, The Macmillan Press LTD., 1983.

[35] R. J. Drago, *Fundamentals of Gear Design*, Butterworth Publishers, 1988.

[36] D. J. Inman, *Engineering Vibration*, Prentice Hall, 1994.

[37] *User Operating Manual for Gearbox Dynamics Simulator.*

[38] R. Tiwari and N.S.Vyas, "Estimation of Non-linear Stiffness Parameters of Rolling Element Bearings from Random Response of Rotor-Bearing Systems," *Journal of Sound and Vibration*, **187**(2), pp. 229-239, 1995.

[39] A. P. Boresi and O. M. Sidebottom, *Advanced Mechanics of Materials*, JOHN WILEY & SONS, INC., 1985.

[40] J. E. Shigley, *Applied Mechanics of Materials*, McGRAW-HILL, INC., 1976.

[41] M. P. Norton, *Fundamentals of Noise and Vibration for Engineers*, Cambridge University Press, 1989.